Thesis for the Degree of Licentiate of Engineering

Ice free roads using hydronic heating pavement with low temperature

Thermal properties of asphalt concretes and numerical simulations

Raheb Mirzanamadi

Department of Civil and Environmental Engineering
Division of Building Technology, Infrastructure Physics

CHALMES UNIVERSITY OF TECHNOLOGY
Gothenburg, Sweden, 2017

Ice free roads using hydronic heating pavement with low temperature
Thermal properties of asphalt concretes and numerical simulations

Lic/Department of Civil and Environmental Engineering
Chalmers University of Technology
Lic 2017:2
ISSN 1652-9146

Department of Civil and Environmental Engineering
Division of Building Technology
Chalmers University of Technology
SE- 412 96 Göteborg
Sweden
Telephone: +46(0)31-772 1000

Cover:
Hydronic heating pavement used to harvest energy from road surface during summer and anti-icing of the surface during winter.

Chalmers Reproservice
Göteborg, Sweden 2017

Ice free roads using hydronic heating pavement with low temperature
Thermal properties of asphalt concretes and numerical simulations
Raheb Mirzanamadi
Department of Civil and Environmental Engineering
Division of Building Technology
Chalmers University of Technology

Abstract

A traditional method to mitigate the slippery conditions of a road is to spread out salt and sand on the road surface. However, salting causes corrosion on the road infrastructures, damage to surrounding vegetation and salification of fresh water. Hence, there is a need for alternative solutions to mitigate the slippery conditions. A renewable alternative is to use a Hydronic Heating Pavement (HHP). The HHP system consists of embedded pipes in the road. A fluid as thermal energy carrier circulates through the pipes. During sunny days, when the road surface is warm, the energy is harvested and saved in seasonal thermal energy storages. During cold days, the warm fluid from the storage is pumped back to the pipes to increase the surface temperature.

The aim of this study is to investigate the performance of the HHP system for harvesting energy from the road surface during summer and anti-icing the road surface during winter. In the HHP system, the main part of the heat transfer occurs between the embedded pipes and the road surface. Hence, it is of importance to determine the thermal properties of the road materials. The thermal properties of a few Swedish typical asphalt concretes, used to construct the asphalt road pavements, were experimentally measured by the Transient Plane Source (TPS) method. The accuracy of the measurements of the TPS method was examined using different sensor sizes. Moreover, in order to investigate the effects of the different design parameters of asphalt concrete such as the types of aggregates on the thermal properties, a numerical model of asphalt concrete was developed. Comparing the obtained thermal properties by the numerical model and the experimental measurements exhibited that the relative error between two methods is in the range of 2% to 10%.

Furthermore, in order to investigate the performance of the HHP system, a two-dimensional numerical model of the HHP system was developed based on the Finite Element Method (FEM). The developed numerical model was validated by two cases: (i) for the road without pipes, using a one year measured data and (ii) for the road with the embedded pipes, using analytical solutions. The validation results for the road without pipes showed that the annual mean difference of the temperature at the depth of 10 cm from the road surface is 0.1°C with the standard deviation of 1.15°C between the measured data and the numerically predicted temperature. The validation results for the road with the embedded pipes showed that the maximum relative error of the thermal resistance between the pipe and surface is less than 5% between the obtained results from the numerical model and the analytical solution.

In order to investigate the harvesting and anti-icing performance of the HHP system, the climate data were selected from Östersund in middle of Sweden, where there is an ongoing test site project to construct the HHP system in 2017. It was assumed that when the road surface temperature was lower than 0°C, the heating was started to keep the surface temperature higher than the dew point temperature. The heating was stopped when the air temperature was below -12°C. Based on the climate data, 90% of the slippery conditions on the road surface, due to condensation, occurred when the air temperature was above -12°C. Furthermore, the air temperature was above 8°C during 70% of the warm days (from the first of May to the end of September). The air temperature of 8°C was taken into account to start harvesting energy from the road surface. The results showed that by maintaining a constant fluid temperature of 6°C through the pipes, 100 mm distance between the pipes and 3.5 m width of the road, the annual required energy for anti-icing the road surface is 356 kWh/(m·year) and the annual harvested energy from the road surface was 1,047 kWh/(m·year). Enhancing the thermal conductivity of the road layers improves the harvesting and anti-icing performances of the HHP system.

Key words: road, slippery condition, hydronic heating pavement, thermal properties, asphalt concrete, finite element method, anti-icing, energy harvesting

Preface

This thesis summarizes the work during two and half years of studies at the division of Building Technology in the research group of Infrastructure Physics at Chalmers University of Technology. The work has been financed by the Norwegian Public Road Administration (Statens vegvessen).

The work has been made possible with the help of Jan Englund and Erick Oscarsson, from Skanska (Road Construction Company) in Gothenburg, who provided and gave advices about asphalt samples. I am grateful for Marek Machowski who helped with technical issues in the laboratory of Chalmers University of Technology.

I want to thank all my colleagues at the division of Building Technology for a good working environment and stimulating discussions, in particularly Josef Johnsson and Sotrios Grammatikos and also my supervisors Bijan Adl-Zarrabi, Pär Johansson and Carl-Eric Hagentoft.

I would also like to thank my friends and family for their supports and especially thanks to Hoda.

Raheb Mirzanamadi
Gothenburg, February 2017

Notations and abbreviations

Symbol	Description	Unit
a	Thermal diffusivity	m^2/s
c	Distance between pipes	m
c_p	Specific heat	J/(kg·K)
D	Embedded depth of pipes from its center to road surface	m
E	Annual required energy	kWh/(m·year)
h_c	Convective heat transfer coefficient	$W/(m^2 \cdot K)$
h_e	Latent heat of water evaporation	kJ/kg
I	Solar irradiation	W/m^2
L	Characteristic length of slab in direction of wind	m
m	Mass per square meter	kg/m^2
$\dot{m}$	Mass flux per square meter	$kg/(m^2 \cdot s)$
M	Mass	kg
p	Water vapor partial pressure	Pa
Pr	Prandtl number	-
q	Heat flow from the pipes	W/m
R	Thermal resistance between the pipes and the surface	m·K/W
R_{pipe}	Pipe radius	m
R_s	Surface thermal resistance	$m^2 \cdot K/W$
Re	Reynolds number	-
RH	Relative Humidity	%
S.D.	Standard deviation	-
t	Time	s
T	Temperature	K, °C
T.Diff	Mean temperature difference	K, °C
u	Mositure ratio (content) mass by mass	kg/kg
v	Wind speed	m/s
V	Volume	m^3
W	Road width	m
x	Horizontal coordinate	m
y	Vertical coordinate	m
z	Height	m
z_0	Roughness lengths for momentum	m

Greek symbols	Description	Unit
β	Moisture transfer coefficient	m/s
υ	Humidity by the volume	kg/m^3
ε	Emissivity coefficient	-
λ	Thermal conductivity	W/(m·K)
ρ	Density	kg/m^3
σ	Stephan-Boltzmann constant	$W/(m^2 \cdot K^4)$
α	Absporptivity coefficient	-
ν	Kinematic viscosity	m^2/s
κ	von Karman constant	-

Subscripts	**Description**
a	Air
ambient	Ambient air
con	Condensation
cond	Conductive heat transfer
conv	Convective heat transfer
dew	Dew point
evp	Evaporation
h	Harvested energy
lw	Long wave radiation
lw-incom	Measured longwave radiation
lowest-air	Air temeprature at which the heating system is stopped
r	Required energy for anti-icing of the road surface
s	Saturated
sw	Short wave radiation

List of papers

This thesis is based on the following papers which are appended:

I. **Raheb Mirzanamadi,** Josef Johnsson, Pär Johansson and Carl-Eric Hagentoft; "Anti-icing of road surfaces using low temperature hydronic heating pavements" To be submitted

II. **Raheb Mirzanamadi**, Pär Johansson, Sotirios Grammatikos; "Thermal properties of asphalt concrete: a numerical and experimental study", To be submitted

Paper I is written by me in collaboration with Josef Johnsson, Pär Johansson and Carl-Eric Hagentoft. The paper covers my work with a numerical model of the Hydronic Heating Pavement (HHP) system to investigate different parameters of the HHP system like pipe distances on the anti-icing performance of the system. I made the numerical model, performed the analysis of the results and wrote the main part of the paper.

Paper II is written by me in collaboration with Sotirios Grammatikos and Pär Johansson. The paper covers my work with measuring thermal properties of different asphalt concrete types using Transient Plane Source (TPS) method and developing a numerical model of asphalt concrete microstructure to investigate the effects of parameters like different aggregate types on the thermal properties of the asphalt concretes. I performed the measurements, made the numerical model and wrote the main part of the paper

The thesis is also based on the following paper which is not appended:

- Adl-Zarrabi, B; **Mirzanamadi, R**; Johnsson, J; Hydronic Pavement Heating for Sustainable Ice-free Roads; Transportation Research Procedia; 2016

Above mentioned paper is written by me in collaboration with Bijan Adl-Zarrabi and Josef Johnsson. The paper covers my work with measuring thermal properties of an arbitrary asphalt concrete at different depths and positions. In the early stage of my PhD, I made a simple model for snow melting using the HHP system which initial results of the model was reported in the paper. I measured the thermal properties and made the snow melting model. The main part of the paper was written by me.

Two other publications by the author are:

a) Adl-Zarrabi, B; Ebrahimi, B; Hoseini, M; Johnsson, J; **Mirzanamadi, R**; Taljegard, M; Safe and Sustainable Coastal Highway Route E39; Transportation Research Procedia; 2016
b) Adl-Zarrabi, B; Johnsson, J; **Mirzanamadi, R**; Hydronic Pavement Using Low Temperature Borehole Thermal Energy Storage; The 2016 World Congress on Advances in Civil, Environmental and Materials Research (ACEM16), Jeju Island, Korea, August 28-September1, 2016

Table of contents

1. Introduction

This section presents: i) the background about the hydronic heating pavement, ii) scope of the study iii) data collection and method, iv) limitations and v) reading guide.

1.1. Background

Norwegian coastal highway route E39, located on the west coast of Norway, connects Kristiansand in the south to Trondheim in central Norway as it is shown in Figure 1-1. The length of the road is 1,100 km. The route E39 links six counties with a total population of 1.8 million (Ellevset 2014). More than half of Norway's energy intensive industry is located along this road. The Ministry of Transport and Communications has given the project "Coastal Highway Route E39" a mandate to address challenges, possible technological solutions and to investigate social and economic benefits of building fixed connections instead of using ferry connections (StatensVegvesen 2016). One example of subjects under investigation is how renewable energy can be harvested by road infrastructures and how the harvested energy can be used in order to reduce the ecological and environmental footprint of the road infrastructures.

Figure 1-1. Coastal highway route E39 in Norway (Ellevset 2014)

The project of "safe and ice free roads using renewable energy" investigates the possibility of utilizing harvested solar energy for deicing the road surfaces during winter to increase road safety. It is well known that driving on a slippery surface could be considered unsafe due to that drivers might lose control of their vehicles. Accidents are more likely when there is a sudden change in the surface friction and this is more common in some sections of the roads such as slopes, curves, bridges and near stretches of water. A traditional method to mitigate the problem of the slippery road conditions is to spread out salt and sand on the road surface. However, consumption of salt and sand for winter maintenance in the Scandinavian countries is over 0.6 million and 1.7 million tons, respectively (Knudsen et al. 2014). Furthermore, salting causes corrosion on the road infrastructures, damage to surrounding vegetation and salification of fresh water (Pan et al. 2015). Considering this high amount of salt and sand consumption along with the negative impacts of salt on the environment and the durability of road infrastructures, there is a need for alternative solutions to mitigate the slippery conditions. A renewable alternative is to use a Hydronic Heating Pavement (HHP) combined with a Seasonal Thermal Energy Storage (STES). The HHP system consists of embedded pipes inside the road. A fluid such as brine (solution of salt and water), oil or glycol-water circulates through the pipes. (ASHRAE 2003). The HHP system harvests solar energy during sunny days, stores it in seasonal thermal energy storages and releases heat for ice/snow melting during cold periods (Liu et al. 2007). A scheme of the HHP system is shown in Figure 1-2.

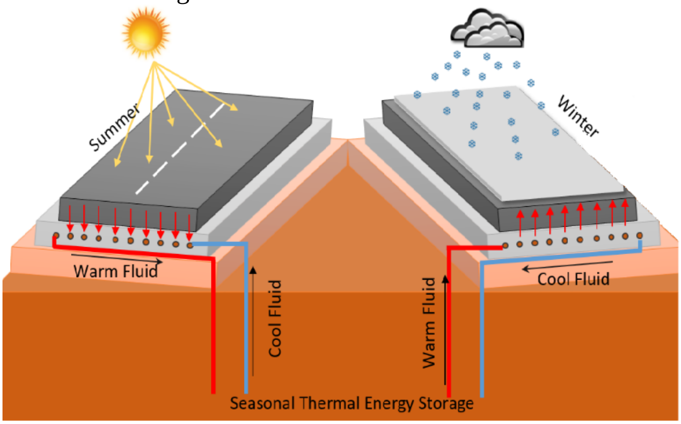

Figure 1-2. Scheme of Hydronic Heating Pavement (HHP) system

Installing the HHP systems in roads is not a new method. In 1948, the earliest system was installed in Klamath Falls, Oregon, USA by Oregon Highway Department. The source of energy in this system was geothermal hot water. This system failed after 50 years of working due to external corrosion of the metal pipes (Pan et al. 2015). Another installed HHP system was the SERSO project in Switzerland, which has been successfully in operation since 1994 (Eugster 2007). The idea of the SERSO project was to defrost a bridge surface using renewable energies and guarantee the same road surface conditions on the heated bridge as on the subsequent road sections. The bridge surface temperature was set just above 0°C to prevent ice formation and freezing of compacted snow (Pahud 2008). The annual runtime of the SERSO project was less than 1,000 hours per year during winter and another 1,000 hours for harvesting energy during summer (Eugster 2007). Additional examples of the HHP systems are the heated sidewalks in Aomori, Japan installed in 2002 and the train platform heating system in Germany installed in 2005 (Eugster 2007). The train platform heating project had the same idea as the SERSO project; i.e. harvesting energy to underground storages during summer and using the stored energy during winter to heat up the train platform (EGEC 2007).

Different pipe materials such as iron, copper and steel were previously used to construct the HHP system (ASHRAE 2003). However, nowadays the plastic pipes are preferred due to avoid the risk of corrosion in metallic pipes (Bobes-Jesus et al. 2013). Furthermore, the size and position of the pipes influence the efficiency of the HHP system. By increasing the pipe sizes as well as installing the pipes closer to each other and to the road surface, the efficiency of the HHP system will increase i.e. the HHP system will enable to melt snow and ice more quickly (Pan et al. 2015). However, by installing pipes at shallower depth, the risk of damage to the pipes will increase. Van Vliet *et al.* (2005) recommended the embedded depth of pipes should be deeper than 50 mm.. In the study done by Dehdezi (2012), it was found that the installation of pipes deeper in the road would reduce the risk of reflective cracking in the asphalt pavement as well as enabling future rehabilitation of the road without damage to the pipe networks. On the other hand, deeper embedded pipes will decrease the efficiency of the HHP system. To compensate the pipe depth problem, a recommended design method is to increase the thermal conductivity of the pavement (Hall et al. 2012). Increasing the thermal conductivity of the road layers leads to an increase in the amount of the heat transfers from the pipes to the road surface.

There has been a number of experimental studies which have demonstrated the possibilities of harvesting energy from pavement solar collectors. In a work by Loomans *et al.* (2003), an asphalt collector in the Netherlands was studied during summer months with mean ambient air temperature of 14°C. They found that the energy efficiency of the asphalt collector was around 30%; i.e. of the incoming solar heat on the road surface nearly 30% could be harvested. The results of another study, which was done for a climate with an annual mean temperature of 4.8 °C, showed that it is possible to harvest about the heat flux of 150 W/m^2 during summer days, using solar asphalt collectors (Gao et al. 2010). Harvesting heat using asphalt solar collector will decrease the road temperature. The reduction of the road temperatures will reduce the plastic deformations such as rutting which in turn will increase the life time of the road (Xu and Tan 2015). Another advantage of cooling down the road surface is to mitigate the effect of Urban Heat Islands (UHI) (Santamouris 2013). UHI is referred to as areas of a city which are considerably warmer than their surrounding areas.

Furthermore, asphalt concrete is widely used to construct the road pavements. In the HHP system, the main part of the heat transfer occurs between the embedded pipes and road surface. Thermal conductivity of asphalt concrete is one of the important parameters that influences the efficiency of the HHP system. The heat delivered to or harvested from the road surface is increasing by using high thermal conductive asphalt concretes. In addition, thermal diffusivity of the asphalt concrete determines how rapidly the heat can transfer from the pipes to the road surface e.g. a low thermal diffusivity leads to a longer time to achieve a certain temperature level on the surface of the road. Hence, accurate determination of thermal properties of asphalt concrete are essential for designing of the HHP system.

1.2. Scope

The aim of this study is to investigate the performance of HHP system for harvesting solar energy from the road surface during sunny days and anti-icing the road surface during cold periods. The influence of the different design options of the HHP systems on the harvesting and anti-icing performance are examined using a numerical simulation model. One of the important parameters which affects the efficiency of the HHP system is the thermal properties of the road materials. The thermal properties of five typical asphalt concretes, used to construct the road pavements in Sweden, are measured. Also, different design parameters of the asphalt concretes, such as aggregate types, are examined to find out their effects on the thermal properties of asphalt concretes. Furthermore, heat transfer interactions between road surface and surrounding climate are analyzed to choose the most suitable boundary condition equations for the road surface. In this study, the fluid temperature, circulating through the pipes, is set to be 6°C during both anti-icing and harvesting periods.

Examples of the research questions in this thesis are:

- What is the energy balance of the road surface using Östersund climate data during harvesting and anti-icing processes of the HHP systems?
- Can the HHP system with low fluid temperatures mitigate the slippery conditions in Östersund?
- What are the effects of design parameters of the HHP system such as thermal conductivity of asphalt concretes on the solar energy harvesting and anti-icing of the road surface using the HHP systems in Östersund?
- What are the thermal properties of some typical asphalt concrete types used to construct different layers of the road such as wearing and binder layers in Sweden?
- How can different design components of an asphalt concrete such as aggregate types and air void contents influence the thermal properties of asphalt concretes?
- Which convective heat transfer coefficient does lead to the best results for the prediction of the road surface temperature?

1.3. Data collection and method

In order to detect the thermal properties of the asphalt concretes, a few asphalt concrete samples were delivered to Chalmers University of Technology by Skanska (Road Construction Company) in Gothenburg, Sweden. The delivered samples were some typical asphalt concrete types used in Sweden to construct asphalt bound layers (wearing, binder and base layers) of the road pavement structure. The thermal properties of these samples were measured using the Transient Plane Source (TPS) method. Moreover, a numerical model of asphalt concrete was developed to investigate the effects of different design parameters of asphalt concretes as well as moisture and freezing conditions on the thermal properties. The numerical models in this study were built in MATLAB R2015b and COMSOL Multiphysics 5.2.

In order to analyze the energy harvesting and anti-icing performance of the HHP system, a numerical model was developed. The numerical model was used to examine the effects of different design options (distance between pipes, embedded depth of pipes, diameter of pipes, thermal conductivity of different layers of road, pipe fluid temperature and the air temperature at which the HHP system stops heating the road surface) on the performance of the HHP system.

Two sets of climate data were used in this study, one set of the climate data was used to validate the numerical model and another set was used to investigate the performance of the HHP system. The first set of the climate data was obtained from a test site in motorway E18 in Sweden (Renman 2016). The data were selected because both climate data and measured temperature of the road, on the surface and different depths, were available. The second set of climate data was related to Östersund area in middle of Sweden and obtained from (Meteotest 2010). Östersund climate was selected because there is an ongoing test site construction of a

HHP system in 2017. The location of the construction site in Östersund and the test-site of motorway E18 are shown in Figure 1-3.

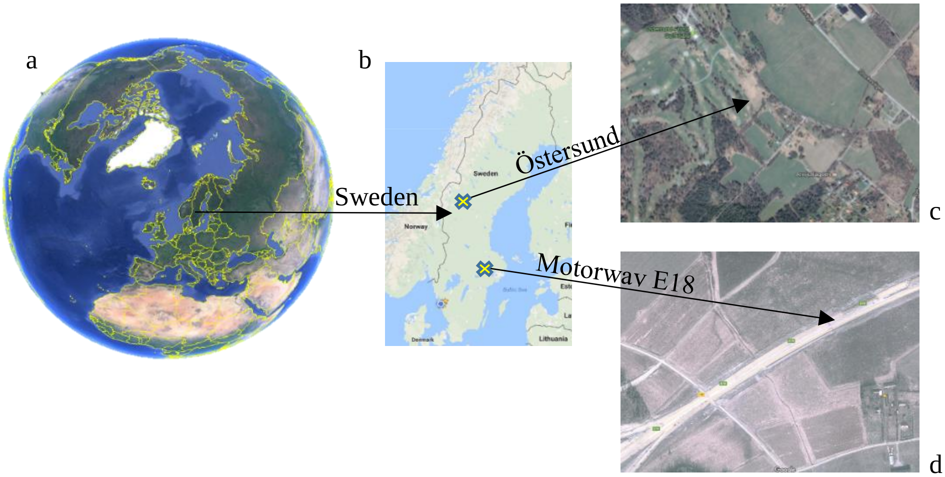

Figure 1-3. Illustration of the locations of (a) Sweden, (b) Östersund and the motorway E18, (c) Östersund planned construction site (d) the motorway E18 test site (Source: https://maps.google.com)

1.4. Limitations

In this work, the developed numerical model of the asphalt concrete microstructure was two-dimensional (2-D). The shapes of aggregates were considered to have a circular cross-section. In addition, all the air voids had the same sizes. The numerical model was validated only using five asphalt concrete types. The effects of moisture saturation and freezing conditions on the thermal properties of asphalt concrete were obtained by the numerical model.

Furthermore, it was assumed that all snow had been plowed away from the road surface, so the investigation was not dealing with snow melting. Also, the slippery condition on the road surface should be mitigated to pass the first coming vehicle. Hence, the produced heats by vehicles such as heat from vehicles engine, exhausted gases and traffic jam are not considered in the heat balances of the road surface.

The performance of the HHP system in this thesis was analyzed based on a fixed fluid temperature. It was assumed that there was no contact resistance between the pipes and asphalt concrete. The road was considered to be made of asphalt materials. Concrete materials were not investigated in this thesis. The emissivity and absorptivity of asphalt concrete were not measured. In addition, the mechanical properties of the road materials were not examined; i.e. installing the HHP system might cause damage to and even collapse of the road. For example, the pipes can be burst under heavy traffic loads. The fluid, circulating through the pipes, will leak into the road, resulting in damage to the road layers. Also, temperature difference between two points of the road, induced by the heating system, can cause thermal cracks.

1.5. Reading guide

In Chapter 2, the experimental method including measurements of thermal properties of asphalt concretes using the TPS methods and moisture uptake are described. In Chapter 3, the development, validation and results of the numerical model of asphalt concrete microstructure are presented. Chapter 4 is about the description of general heat transfer mechanisms on road surfaces and the selection of the most suitable model for the convective heat transfer coefficient and sky temperature. Chapter 5 is about developing numerical model of the HHP system and the validation of this model using measured data and analytical solutions. Finally, Chapter 6 presents the results of the numerical model for the energy harvesting and anti-icing performance of the HHP system.

2. Experimental tests to determine thermal properties

There are various experimental methods which are used to determine the thermal properties of materials. Some of these methods and their results for asphalt concrete are shown in Table 2-1.

Table 2-1. Experimental methods used to measure the thermal properties of asphalt concretes

Reference	Method	Results
Luca and Mravira 2005	Guarded thermal testing device, designed and developed at the University of New Brunswick, Canada (the UNB k-alpha tester).	Thermal conductivity of laboratory compacted superpave hot-mixed asphalt was observed to vary from 1.4 W/(m·K) to 2.1 W/(m·K) for dense graded mixtures. Thermal diffusivity was observed to range from $0.44\cdot 10^{-6}\ \mathrm{m^2/s}$ to $0.64\cdot 10^{-6}\ \mathrm{m^2/s}$
Michael S. Mamlouk et al. 2005	Asphalt concrete sample was placed in a chamber which the changes of temperatures at different positions of the sample were monitored during measurement. The shape of sample was cylindrical in the dimensions of 100 mm diameter and 150 mm thickness.	Thermal conductivity of asphalt materials varied between 0.7 W/(m·K) and 1.4 W/(m·K). Thermal diffusivity was observed to range from $0.42\cdot 10^{-6}\ \mathrm{m^2/s}$ to $2.7\cdot 10^{-6}\ \mathrm{m^2/s}$.
Xu and Solaimanian 2010	Asphalt concrete sample was placed in a dual chamber which the changes of temperatures at different positions of the sample were monitored during measurement. The shape of sample was cylindrical in the dimensions of 150 mm diameter and 165 mm thickness.	The bitumen content and air void content were 4.7%, 5.8%. The density of the asphalt concrete sample was 2313 kg/m^3. The crushed aggregate was from a limestone with 19 mm nominal maximum aggregate size. The thermal conductivity of 2.88 W/(m·K) and the thermal diffusivity of $1.42\cdot 10^{-6}\ \mathrm{m^2/s}$ were attained from the back-calculation
Chen et al. 2012	Transient Plane Source (TPS)	Thermal conductivity of asphalt materials varied from 1.37 W/(m·K) to 1.54 W/(m·K) and the thermal diffusivity varied from $0.55\cdot 10^{-6}\ \mathrm{m^2/s}$ to $0.69\cdot 10^{-6}\ \mathrm{m^2/s}$
Côté et al. 2013	Thermal conductivity cell (steady-state method). The shape of asphalt concrete sample was cylindrical in the dimensions of 100 mm diameter and 75 mm thickness. The sample was placed between two heat exchangers. Heat fluxes were measured at both ends of the sample.	Density of samples varied from 2,316 kg/m^3 to 2,468 kg/m^3. Thermal conductivity of asphalt materials varied from 1.16 W/(m·K) to 1.82 W/(m·K).

As can be seen in Table 2-1, the most frequently used method to determine the thermal properties of asphalt concretes is the steady-state method. However, the measurement process by steady-state method requires long time (up to several hours for each sample). Furthermore, setting up the steady-state conditions needs a specific size of asphalt concrete samples depending on the measurement method. For example, available guarded heat flow meter at Chalmers University of Technology requires sample size of 300 mm x 300 mm (sample thickness should be smaller than 70 mm). The delivered asphalt samples by Skanska (Road Construction Company) were not large enough to use this method. In this study, instead, a transient method was selected to measure the thermal properties of the asphalt concrete samples. The required time of each measurement was less than 5 minutes. The measurements were done using the Transient Plane Source (TPS) technique. According to Gustafsson (2013), the accuracy of the TPS method to measure the thermal conductivity of whole range of materials is within +/- 5%.

2.1. Transient Plane Source (TPS) method

Transient Plane source (TPS) method was introduced by Gustafsson (1991) for the measurement of thermal conductivity and diffusivity of solid materials. The method is based on the use of a transiently heated plane sensor. The TPS sensor is made in the shape of a double spiral which is etched out of a thin nickel metal. The double spirals sandwich between two layers of thin kapton (insulating material). For a typical measurement, a sensor is clamped between two pieces of the (same) material under investigation. The TPS sensor is employed as both a heat source and an electric resistance thermometer. A constant electrical current is injected through the sensor for a fixed period of time. The generated temperature difference between the two sample pieces is recorded by the sensor. The rate of temperature increase depends on the material types; i.e. how the produced heat by the sensor could conduct inside the materials. The variation of temperature with time is used to calculate the thermal conductivity and diffusivity of the materials. Furthermore, in the TPS technique, it is assumed that the sensor is located in an infinite medium. Therefore, the measurement time should be controlled so that the thermal penetration depth (generated during measurement) does not exceed the thickness of the tested sample. Figure 2-1 illustrates an example of the TPS sensor, position of the sensor on the asphalt surface and clamping sensor between two pieces of asphalt concrete samples. More information about the measuring process by the TPS can be found in (Gustafsson, 2013).

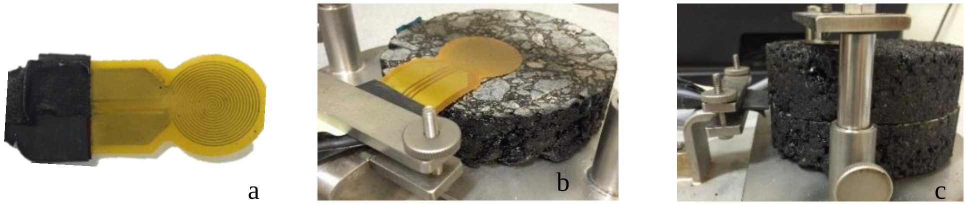

Figure 2-1. Using Transient Plane Source (TPS) method to measure the thermal properties of the asphalt concrete (a) an example of the TPS sensor, (b) the TPS sensor position on the surface of an asphalt sample and (c) employing the sensor between two halves samples
(Photos: Raheb Mirzanamadi)

2.2. Determining thermal properties of asphalt concrete samples at different positions and depths

The measurement of the thermal properties of asphalt concrete started with a cylindrical sample with the radius of 100 mm and thickness of 60 mm, which was arbitrary selected by Skanska (Road Construction Company) in Gothenburg. The TPS method needed two identical specimens, thus the sample was cut from height into two specimens with a thickness of 30 mm. Furthermore, the specimens were cut again from height into two new specimens to measure the thermal properties at different depths. It is important to note that in this study, it is assumed that the two specimens of the asphalt concretes were symmetrical and identical. The samples were conditioned in the laboratory. The temperature and Relative Humidity (RH) in the laboratory were 22°C and around 50%, respectively. Figure 2-2 shows the surface of the sample and positions of the measurement.

The initial sample used in the measurement was arbitrary selected; thus, the information about its binder and aggregate was missed. However, the largest aggregate size was 11 mm.

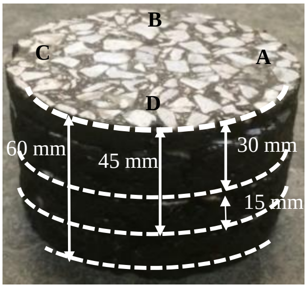

Figure 2-2. Measuring thermal properties of an arbitrary asphalt sample at four positions of A-D and at two different depths of 30 mm and 45 mm (Photo: Raheb Mirzanamadi)

In order to investigate the thermal properties of the asphalt sample at different positions and depths, two different measurement setups were used. In the first setup, the thermal properties were measured at four different positions over the sample surface, see Figure 2-2. In the second setup, the thermal properties were measured at different depths i.e. 30 mm and 45 mm from the sample surface. According to the recommendation for performing the TPS measurements, the thickness of the sample under investigation should be at least equal to the radius of the TPS sensor (Gustafsson 2013). Thus, in order to not jeopardize the accuracy of the measurement, the sensor with the diameter of 19.7 mm was selected. The results of the measured thermal properties at different positions and depths are presented in Table 2-2.

Table 2-2 Thermal properties of the arbitrary asphalt pavement at four different positions and two different depths (Adl-Zarrabi, et al. 2016)

Position	Depth (mm)	Conductivity (W/(m·K))	Diffusivity (mm^2/s)	Volumetric heat capacity ($MJ/(m^3K)$)
A	30	2.38	1.39	1.71
	45	2.49	1.45	1.71
B	30	2.39	1.38	1.73
	45	2.54	1.49	1.70
C	30	2.67	1.28	2.07
	45	2.66	1.49	1.78
D	30	2.43	1.32	1.84
	45	2.57	1.21	2.13

As can be seen in Table 2-2, the thermal conductivity of the asphalt concrete sample at the depth of 30 mm and at three positions of A, B and D are in the same range with the maximum deviation of 2%. Furthermore, the diffusivity and volumetric heat capacity of the sample at positions A, B and D are in the same range with a deviation of about 5%. However, the thermal diffusivity, thermal conductivity, and volumetric heat capacity of the sample at the position C in comparison with the other positions deviate by 8%, 10% and 20% respectively. A reason for the deviation might be the inconsistent distribution of the aggregates in the asphalt sample. However, if the size of the sensor was large enough, the deviation between the different positions would be eliminated. The variations of measured thermal properties at two different depths of 30 mm and 45 mm from the sample surface for conductivity, diffusivity and volumetric heat capacity are about 6%, 14% and 14%, respectively. The deviation of the thermal properties at two different depths might happen because of two main reasons: the different aggregate distributions and also the different compaction pressures. Further investigation was done in Section 2.3 in order to examine the effects of different sensor sizes on the TPS measurements to determine the thermal properties of asphalt concrete.

2.3. Effects of the TPS sensor sizes on the accuracy of the measured thermal properties of asphalt concrete

In this section, the different TPS sensor sizes were investigated in order to select the most suitable sensor size with regard to the maximum aggregate size of the asphalt concrete samples. In the initial stage of the investigation, three different types of asphalt concrete samples (ABT11, ABS11 and AG22) were provided by Skanska. The samples were in the dimensions of 100 mm diameter and 60 mm thickness. The mean weights of ABT11, ABS11 and AG22 were 1,217 g, 1,151 g and 1,169 g, respectively. Penetration grade of the bitumen used to make ABT11 and ABS11 was 70/100 and that to make AG22 was 100/150. Penetration grade assesses the suitability of the bitumen for use under different climate conditions and measured in 0.1 mm (Huang Yang, 2008). All samples were fabricated by use of the standard Marshal Compaction method. Three specimens of each type of asphalt concrete sample were delivered in one week to Chalmers University of Technology after construction in the laboratory. The scheme of different types of asphalt concrete samples is shown in Figure 2-3.

All of the asphalt samples were cut from depth into halves in order to measure their thermal properties, see Figure 2-1(c). In order to improve the accuracy of the measurements, the thermal properties were acquired at two random positions. Also, three measurements were recorded at each position. Finally for each type of asphalt concrete sample (e.g. ABT11), the mean value of the total of 18 measurements (three specimens, two positions and three measurement for each position) was used to report the thermal property of each sample. The waiting time between two successive measurements was at least 20 minutes.

Before starting the measurements of thermal properties by the TPS method, asphalt concrete samples were stored (pre-conditioned) for three weeks in room conditions with the temperature of 22℃ and 30% RH. Then, the effects of different sensor sizes on the estimation of thermal properties of asphalt concrete were investigated. Table 2-3 tabulates the i) sensor design ID, ii) sensor diameter, iii) implemented power in TPS and iv) measurement time. It is important to note that the thickness of the sample is larger than the maximum thermal penetration depth, generated during the measurement. An estimation of the penetration depth is calculated as $2 \cdot \sqrt{a \cdot t}$. Here, a (m^2/s) is the thermal diffusivity and t (s) is the measurement time of the experiment by the TPS method. For more information, the reader is referred to (Gustafsson, 2013).

Table 2-3. Details related to each sensor size for measuring the thermal properties of asphalt concretes using the TPS method (from paper II)

Sensor design ID	Sensor diameter (mm)	Power (mW)	Measurement time (s)
5465	6.36	100	10
5501	12.8	200	40
8563	19.7	300	80
4922	29.2	1000	160
5599	58.8	1000	320

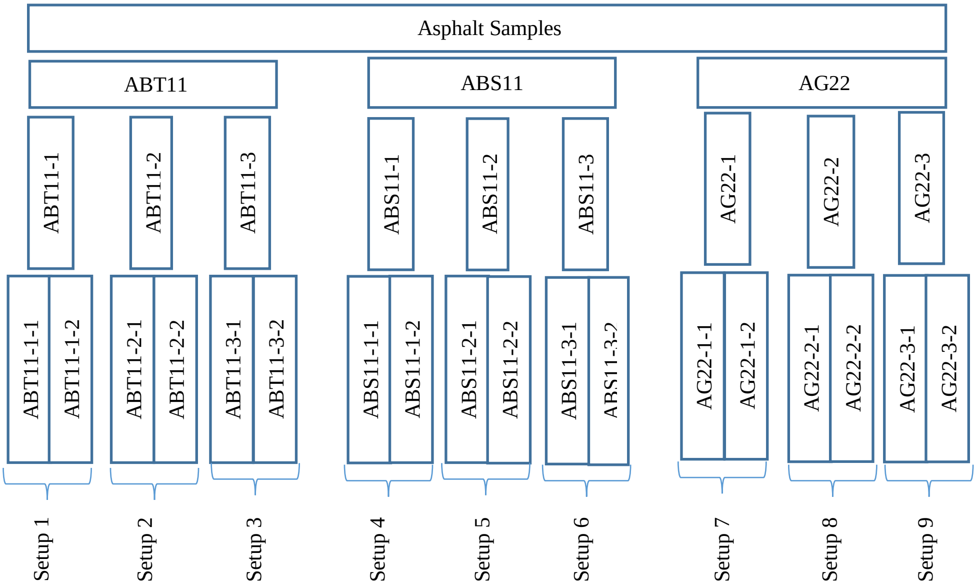

Figure 2-3. The schematic picture of different types of asphalt concrete samples used to examine the effects of different sensor sizes of the TPS method on the measurement of the thermal properties of asphalt concrete samples

The different TPS sensor sizes were employed to examine their effect on the measurement of thermal properties. The effects of the sensor size vs. the maximum aggregate size ratio on the thermal conductivity and thermal diffusivity values are presented in Figure 2-4. As shown, a variation in the thermal properties is recorded by using the different sensor sizes. When the sensor diameter to the maximum aggregate size ratio is less than 2, a significant variation between the measured thermal properties occurs. Small sensor sizes, covering small measuring areas, often lead to inaccurate measurements e.g. the measured thermal conductivity of AG22 is 25% higher by the sensor size with the diameter of 6.36 mm than that measured by the sensor size with the diameter of 58.8 mm. It is highly likely that the thermal reading of the small size sensor (6.36 mm diameter) reflects mostly the thermal properties of aggregates. On the other hand, a large size sensor (58.8 mm diameter) is large enough to cover both aggregate and binder fractions, allowing for more accurate measurements. By increasing the sensor size to maximum aggregate size ratio the variations in the measured thermal conductivity and diffusivity values are minimized. When the ratio exceeds 2, the variation of thermal properties (apart from the thermal diffusivity of ABS11) is less than 4%. ABS11 consists of about 70% quartzite (coarse aggregate) and 30% diabase (fine aggregate), a non-uniform distribution of which might be the cause of encountered oscillation in the thermal properties when using different sensors. In such design case, it is recommended to employ large size sensors.

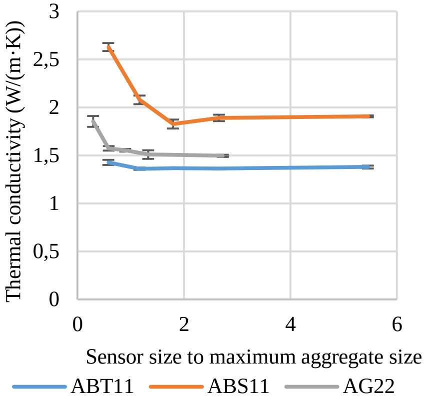

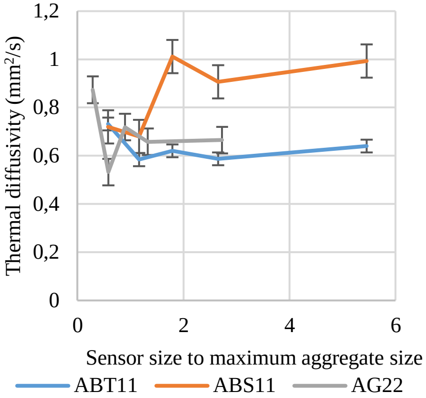

Figure 2-4. The effects of the ratio of sensor diameter to the maximum aggregate size on (a) the thermal conductivity of asphalt concrete and (b) thermal diffusivity of asphalt concrete. The vertical bars show the standard deviations of 18 measurements (from paper II)

2.4. Thermal properties of five types of asphalt concretes

In Sweden, ABT11, ABS11 and ABS16 are some typical asphalt concrete types for the construction of the first layer (wearing layer). ABB22 is a typical type of asphalt concrete to construct the second layer (binder layer). In addition, AG22 is typically used to construct the third layer (base layer). Details of each sample type are tabulated in Table 2-4. The presented details are the (i) bitumen content, (ii) air void content, (iii) asphalt concrete density, (iv) aggregate types and (v) amount of aggregates passed from different sieve sizes.

All types of asphalt concrete samples had cylindrical shape in the dimensions of 60 mm thickness and 100 mm diameter. The samples were cut through thickness into two pieces, the same as Figure 2-1 (c). By selecting the sensor size with the diameter of 29.2 mm, the thermal properties of all mentioned samples were measured using the TPS method. The measurement process was the same as Sections 2.2 and 2.3. The results of measured thermal properties of different asphalt concrete types using the TPS method are shown in Table 2-5.

2.5. Effects of moisture on the thermal properties of asphalt concrete

This section presents the effects of moisture on the thermal properties of an asphalt concrete. In general, the moisture can be transported in three different ways into the porous materials, namely i) diffusion, ii) capillarity flow and iii) hydraulic flow (Apeagyei et al. 2014). If the moisture content of a material is in the hygroscopic region (0–95% RH), the main part of the moisture will be transported into the materials by the diffusion. In this study, only the diffusion state with dry materials is taken into consideration. The study is done in accordance with ASTM D5229 (ASTM standard 2010) and the work done by Apeagyei *et al.* (2014).

Table 2-4. Details associated with asphalt concrete samples, used in Sweden for construction road pavements (The data were provided by Skanska (Road Construction Company) in Gothenburg)

Sieve size (mm)	ABT11	ABS11	ABS16	ABB22	AG22
	Bitumen content: 5.8% Air content: 2.1% Density: 2,617 kg/m^3 All aggregates are Diabase	Bitumen content: 6.6% Air content: 2.8% Density: 2,421 kg/m^3 Aggregates> 4 mm are quartzite, Aggregates < 4 mm are Diabase	Bitumen content: 6.4% Air content: 1.7% Density: 2,415 kg/m^3 Aggregates> 4 mm are quartzite, Aggregates <4 mm are Diabase	Bitumen content: 4.9% Air content: 3.6% Density: 2,577 kg/m^3 All aggregates are Diabase	Bitumen content: 4.1% Air content: 4.9% Density: 2,582 kg/m^3 All aggregates are Diabase
	Amount of aggregates passed from different sieve sizes				
31.5	100	100	100	100	100
22.4	100	100	100	100	97
16	100	100	97	79	76
11.2	98	96	57	48	57
8	77	51	38	33	44
5.6	62	36	30	29	37
4	50	30	27	26	30
2	34	25	23	22	21
1	24	19	19	17	15
0.5	18	15	16	14	12
0.25	14	14	14	10	9
0.125	9	11	11	7	7
0.063	7.7	9.3	7.8	4.6	5.3

Table 2-5. Thermal properties of different asphalt concrete types measured by the TPS methods (S.D.: Standard Deviation)

Model	ABT11	ABS11	AG22	ABS16	ABB22
Thermal conductivity (W/(m·K))	1.39	1.89	1.51	2.24	1.44
S.D. for Thermal conductivity (W/(m·K))	0.01	0.03	0.05	0.03	0.03
Volumetric heat capacity (MJ/(m^{3}K))	2.16	2.08	2.25	2.05	2.21
S.D. for Volumetric heat capacity (MJ/(m^3·K))	0.06	0.09	0.09	0.13	0.07
Thermal diffusivity (mm^2/s)	0.64	0.91	0.67	1.1	0.65
S.D. for Thermal diffusivity (mm^2/s)	0.02	0.01	0.05	0.07	0.03

Moisture uptake is the measure or ability of a hygroscopic material to absorb moisture when exposed to air with a given RH. If M_{dry} (kg) is the mass of a material at its dry condition and M_t (kg) is the mass of the material after a given exposure time, then the moisture content, u (%), after time t can be calculated as:

$$u(\%) = \frac{M_t - M_{dry}}{M_{dry}} \times 100 \qquad (2\text{-}1)$$

The wearing layer is always exposed to environmental conditions during service time i.e. ambient air moisture, rain and freezing. The different environmental conditions could affect the thermal properties of asphalt concrete. Therefore, the investigation of the moisture uptake behavior is critical for the assessment of the performance of asphalt concrete. The objective of this section is to investigate the effects of different RH levels on the thermal properties of the wearing layer. In Sweden, ABT11 is a commonly used type of asphalt concrete for the wearing layer. Hence, this type of asphalt concrete was selected as the target sample in this study.

The thermal properties of the ABT11 samples were measured by the TPS method in three different conditions. At first, the samples were conditioned in a room at 22°C and 50% RH for two months. Then, they were dried in an oven at 35°C for 19 days. Finally, the samples were conditioned at 22°C and 93% RH for 71 days. The details related to the conditioning of the samples are presented in paper II, Section 4.4.

Figure 2-5 illustrates the moisture content of the ABT11 samples when they were exposed to the RH levels of 50% and 93%. For practical reasons in this work, it is assumed that when the change in moisture content in a time-window of 24 hours is less than 0.02 g (two times of the sensitivity of the balance used in this study), the moisture content is in equilibrium state. That said, mean equilibrium moisture content of ABT11 samples is 0.03 % at 50% RH and 0.26% at 93% RH. Considering the mean dried weights of the ABT11 samples as 1,217.33 g, the absorbed moisture for the ABT11 at 50% RH is 0.37 g and at 93% RH is 3.17 g.

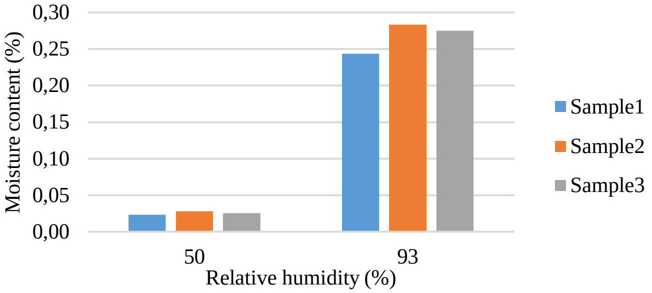

Figure 2-5. Moisture content of the ABT11 samples exposed to air with 50% RH for 19 days and to 93% RH for 71 days

The measured thermal properties of the ABT11 samples at the different RH levels and oven dried condition are shown in Table 2-6. As can be seen, exposing the ABT11 samples to 93% RH does not prove any significant variation in the thermal properties of the asphalt concrete, compared to 50% RH and dried condition. The maximum variation among the measured thermal properties is less than 5%. This variation is related to the thermal diffusivity of the ABT11 between the RH levels of 50% and 93%. The ABT11 sample is a dense asphalt concrete with 2.1% air void content. This low air void content could be one reason that exposing the ABT11 to a high RH level does not lead to any significant change in the thermal properties.

In addition, the results do not show a consistent trend in the thermal properties by changing the RH levels. It is worth mentioning that for each measurement, the position of the TPS sensor between two clamped half samples of asphalt concrete was randomly selected to let the sensor cover different areas on the asphalt concrete surfaces. The random position could be another reason of the inconsistent trend.

Table 2-6. Thermal properties of ABT11 in saturation and different RH

Relative humidity level	**93%**	**50%**	**dried**
Thermal conductivity (W/m·K)	1.40	1.36	1.39
S.D. for Thermal conductivity (W/m·K)	0.01	0.02	0.02
Volumetric heat capacity (MJ/m^{3}K)	2.15	2.19	2.16
S.D. for Volumetric heat capacity (MJ/m^{3}K)	0.08	0.13	0.06
Thermal diffusivity (mm^2/s)	0.65	0.62	0.64
S.D. for Thermal diffusivity (mm^2/s)	0.02	0.04	0.02

3. Numerical model to estimate the thermal properties of asphalt concretes

Asphalt concrete in the micro-scale level is a heterogeneous medium which consists of a random distribution of aggregates, fillers and bitumen. However, in the macro-scale, the constituents are assumed to be homogeneously distributed, forming an isotropic structure. Hence, it is of importance to characterize a single “effective” thermal conductivity that represents the heterogeneous conductivities of all the constituents. The process is known as homogenization (Karim and Krabbenhoft 2010). In this thesis, a numerical model is developed to determine the effective thermal conductivity of asphalt concretes. The effective thermal conductivity can be calculated with Fourier’s law as:

$$\lambda = -\frac{q \cdot L}{\Delta T} \tag{3-1}$$

where λ (W/(m·K)) is the effective thermal conductivity, q (W/m^2) is heat flux, L (m) is the thickness of the sample and ΔT (K) is the temperature difference between two opposite sides of the sample. It is also assumed that the thermal conductivity of asphalt concrete is not affected by temperature (the thermal conductivity is treated as constant).

The thermal diffusivity of a material represents how rapidly heat can flow inside a material. The thermal diffusivity of a material can be calculated as:

$$a = \frac{\lambda}{c_p \cdot \rho} \tag{3-2}$$

where a (m^2/s) is the thermal diffusivity and $c_p \cdot \rho$ (MJ/(m^3·K)) is the volumetric heat capacity. The volumetric heat capacity characterizes the ability of a given volume of a material to absorb energy while experience a given temperature change. $c_p \cdot \rho$ of asphalt concrete can be calculated as the sum of the volumetric heat capacities of each component multiplied by their volumetric proportion in the composite (Dehdezi, 2012).

$$c_p \cdot \rho = \frac{(c_p \cdot \rho \cdot V)_{aggregate} + (c_p \cdot \rho \cdot V)_{bitumen} + (c_p \cdot \rho \cdot V)_{moisture} + (c_p \cdot \rho \cdot V)_{air}}{V_t} \tag{3-3}$$

where c_p (J/(kg·K)) is the specific heat capacity, ρ (kg/m^3) is the density, V (m^3) is the volume of each component and V_t (m^3) is the total volume of the asphalt concrete.

A common method to generate the microstructure of asphalt concrete is a hierarchically-based multiscale approach. As such, the generated structure by smaller aggregates is regarded as a component of the next structure composed of larger aggregates e.g. the structure generated of bitumen and aggregates smaller than 0.063 mm is regarded as binder for asphalt concrete composed of aggregates between 0.063 mm and 11 mm. Previous studies (Chen et al. 2013; Chen et al. 2015), as it is shown in Figure 3-1 (a), employed several matrixes to generate the final asphalt sample to calculate thermal conductivity values. However, this process exhibited reduced accuracy in the computed results and required several simulation efforts. In this thesis, in order to increase the accuracy of the results (taking into consideration mechanical interlocking and contact among different aggregates) and also reduce the simulation process efforts, the asphalt concrete microstructure (including all aggregate sizes larger than 0.063 mm) is generated for only one sample. The scheme of the generating microstructure using a hierarchical multiscale method is shown in Figure 3-1 (b).

3.1. Numerical generation of asphalt concrete microstructure

In this thesis, the method of random distribution programming was used to numerically generate the microstructure of asphalt concrete samples. This method made it possible to investigate the effects of different design parameters like different binder types on the thermal conductivity of the asphalt concrete. It is worth noting that according to (Chen et al. 2013), when the aggregates were randomly distributed, the aspect ratio of aggregates had little effect on the thermal conductivity of asphalt concrete. Therefore, in this thesis, the shapes of the aggregates were considered to have a circular cross-section. Furthermore, despite the fact that a real asphalt concrete sample is three-dimensional (3-D) considering the required huge time consumption and computational resources of generating 3-D models, this study instead followed a development of a two-dimensional (2-D) numerical model approach.

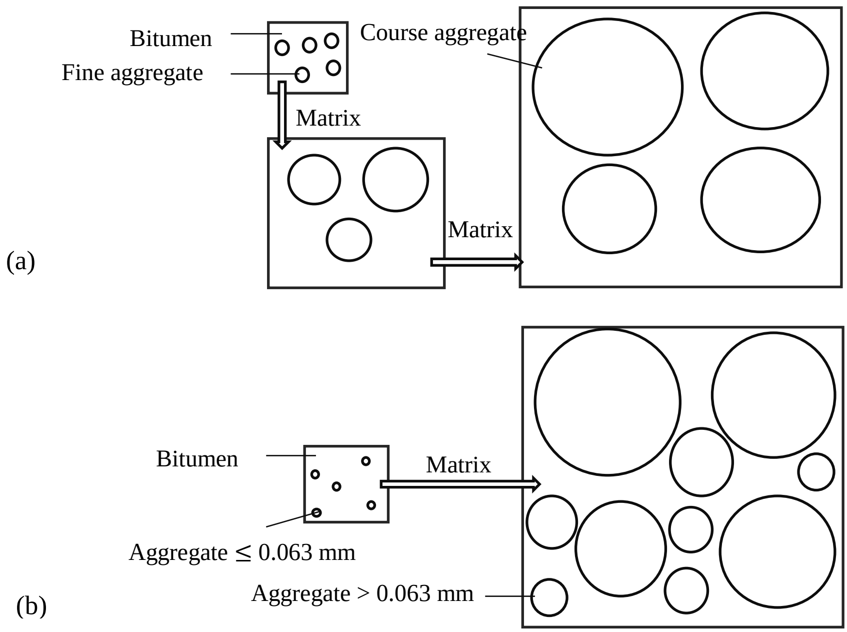

Figure 3-1. Scheme of generating aggregate microstructure using a hierarchical multiscale method (a) generating different matrix to reach the final sample (b) the generated microstructure model in this thesis using only one matrix

The volumetric size of each component is of primary importance in order to generate the microstructure of an asphalt concrete sample. However, as can be seen in Table 2-4, in all of the delivered asphalt samples to Chalmers University of Technology, only air void content is based on the volumetric rate. The other contents are based on mass rate. Therefore, prior to any calculation, it is required to convert mass ratio to volume ratio for each individual component.

The equations related to the conversion of mass ratios to volume ratios are presented in paper II, Section 2.1.

The generation process using random distribution programming was performed in MATLAB R2015b. Details are as follows:

1. The amount of different aggregates were calculated for a square of 60 mm side length size. This length was approximately five times larger than the largest aggregate size of ABT11 and ABS11 samples. The largest aggregate size of these samples was 11.2 mm, see Table 2-4.
2. The generation of aggregates started from the larger to the smaller size. To speed up the process, after generating and randomly placing an aggregate, the placed area was 'booked' and no more random aggregate could be generated and take the same place.
3. A control system was posed on generated aggregates to avoid overlapping with other aggregates. In the case of overlapping an aggregate with others, its position was removed and a new position was randomly selected. The process continued until zero overlapping.

An example of generated asphalt concrete sample is shown in Figure 3-2 (a). As it is seen, the edges of the sample mostly consisted of fine aggregates due to random positioning of the aggregates. This form of distribution of the aggregates could affect the accuracy of the calculated effective thermal conductivity. Hence, in order to consider the contribution of coarse aggregate in the calculation of effective thermal conductivity and reduce the computational cost of the calculation, a square (A_{total}) of 30 mm side length size was extracted from the generated area as the final sample. 30 mm length was selected to hold sample's length larger than the largest possible aggregate size (22.4 mm) so as to accurately calculate the thermal properties. An example of length downsizing of generated asphalt concrete sample is shown in Figure 3-2 (b).

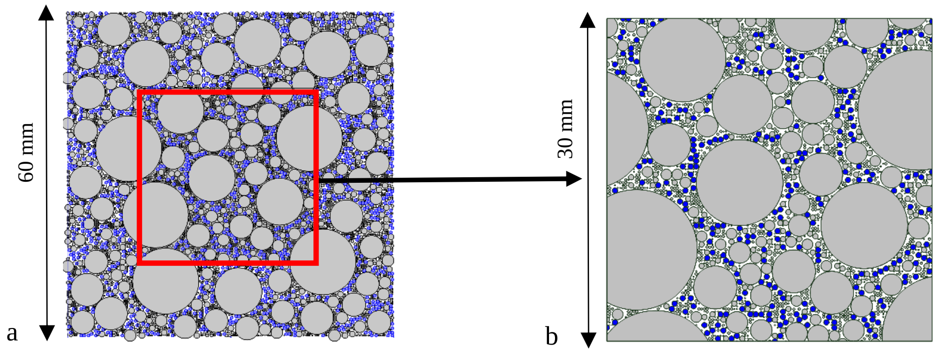

Figure 3-2. A generated asphalt concrete sample. Gray circles represent aggregates, blue circles represent air voids and white area represents the binder (bitumen and filler) (a) initially generated asphalt concrete sample with the length of 60 mm (b) final generated asphalt concrete sample with the length of 30 mm extracted from the initial sample (from Paper II)

3.2. Validation of the numerical model of asphalt concrete

In this section, the thermal properties derived experimentally (using the TPS method) in Table 2-5 are compared with the thermal properties predicted through the developed numerical model. In order to detect the thermal properties of asphalt concrete, the thermal properties of the different constituents were derived from the literature and used as input in the numerical model. Thermal properties of different components are presented in Table 3-1.

Table 3-1. Thermal properties of different components (from paper II)

Reference	Component	Thermal conductivity (W/(m·K))	Density (kg/m^3)	Specific heat capacity (J/(kg·K))
Pan et al. 2014	Binder	0.37	1459	1158
Theodore L. et al. 2011	Stagnant air* (22°C)	0.025	1.18	1017
Côté et al. 2013; Andolfsson 2013; Robertson 1988	Quartzite aggregate	5	2650	850
Côté et al. 2013; Andolfsson 2013; Robertson 1988	Diabase aggregate	2.30	2980	817

* Radiative heat transfer among the pore walls of the asphalt concrete samples is taken into account by Equation 2 in paper II.

The effective thermal conductivity, λ (W/(m·K)), for the samples was calculated at steady-state condition. For each type of asphalt concrete, three various numerical samples were generated. In addition, for each sample, as it is shown in Figure 3-3, λ was calculated at two perpendicular directions. By having the average heat flux, q (W/m^2), temperature difference, ΔT (K), in two opposite boundaries of the sample and length of the sample, L (m), the value of λ were calculated using Equation 3-1. For each sample, the thermal diffusivity and volumetric heat capacity were calculated through Equations 3-2 and 3-3, respectively. The thermal properties of asphalt concrete obtained by the experimental and numerical methods are tabulated in Table 3-2. The relative error is defined as the difference between the thermal properties obtained by experimental method and numerical model divided by the experimental results. The mean relative error in this study is between 2% and 10%.

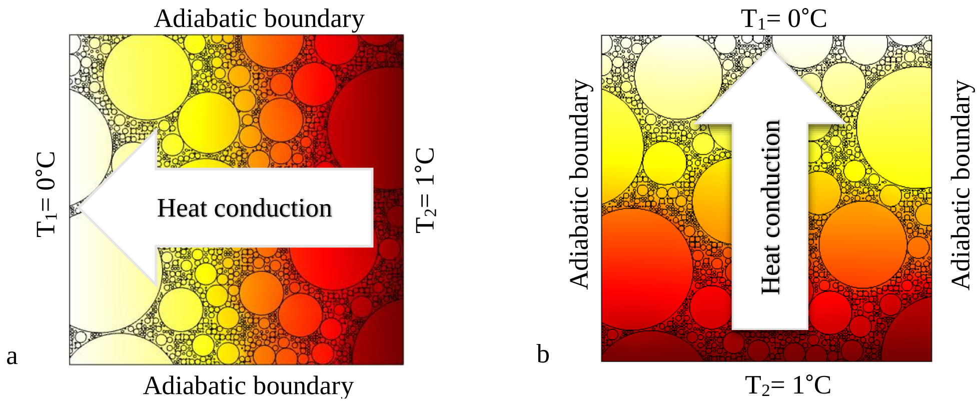

Figure 3-3. Steady-state heat transfer is applied to the numerically generated asphalt concrete by setting two different constant temperatures in (a) left and right boundaries (b) upper and bottom boundaries

For the sake of comparison, the thermal conductivity of the different asphalt concrete types are predicted using both empirical and analytical models. The results are shown in Table 3-3. The analytical models used in this work to determine the thermal conductivity are the parallel and series models (Hagentoft 2001) as well as the checkerboard model (Karim and Krabbenhoft 2010). Furthermore, the empirical model used to predict the thermal conductivity was obtained from (Côté et al. 2013). The model details can be found in the corresponding literature.

Table 3-2. Thermal properties of asphalt concrete obtained from numerical and experimental methods

Asphalt types		Thermal conductivity (W/m·K)	Volumetric heat capacity (MJ/m^{3}K)	Thermal diffusivity (mm^2/s)
ABT11	Experimental	1.39	2.16	0.64
	Numerical	1.29	2.23	0.58
	Error (%)	7.19	3.24	9.37
ABS11	Experimental	1.89	2.08	0.91
	Numerical	2.02	2.11	0.96
	Error (%)	6.87	1.44	5.49
AG22	Experimental	1.51	2.25	0.67
	Numerical	1.47	2.31	0.64
	Error (%)	2.64	2.68	4.47
ABS16	Experimental	2.24	2.05	1.1
	Numerical	2.07	2.13	0.97
	Error (%)	7.58	3.90	11.8
ABB22	Experimental	1.44	2.21	0.65
	Numerical	1.41	2.31	0.61
	Error (%)	2.08	4.52	6.15

Table 3-3. Thermal conductivity of five different asphalt concrete samples using experimental, numerical, analytical and empirical models

Model	ABT11	ABS11	AG22	ABS16	ABB22
Experimental results	1.39	1.89	1.51	2.24	1.44
FEM in this thesis	1.29	2.02	1.47	2.07	1.41
Parallel	1.98	3.64	1.97	3.74	1.94
Checkboard	1.33	1.48	1.28	1.47	1.27
Series	0.62	0.57	0.36	0.76	0.36
Empirical model	1.37	1.73	1.17	2.39	1.26

The mean relative errors between predicted values using various models and the experimental data are shown in Table 3-4. Of all models, the model developed based on the Finite Element Method (FEM) has the best fit with the experimental data, while the series model results in the maximum relative error. The order of accuracy for different models is observed as FEM model > Empirical model > Checkboard model > Parallel model > Series model. Empirical model proposed by Côté et al. (2013) has 10% mean relative error in comparison with the experimental results. This model could be used as a quick prediction tool for detecting the thermal conductivity of the asphalt concrete.

Table 3-4. Mean relative errors between predicted and experimental results of the thermal conductivity of five different types of asphalt concretes

Model	Mean relative error (%)
FEM in this thesis	4.59
Parallel	54.50
Checkboard	16.77
Series	68.16
Empirical model	10.48

3.3. Effects of graphite as a filler in the binder

This section presents the effects of graphite on the thermal conductivity of asphalt concrete samples. The information associated with the thermal properties of the graphite-modified binder is obtained from the literature (Pan et al. 2014) and is presented in Figure 3-4. The graphite consisted of 98.9% carbon, 0.2% ash and 0.03% iron by weight. Its particle size was less than 150 µm. Graphite's thermal conductivity was 59.32 W/(m·K). The results were obtained from experimental measurements. More information can be found in the literature (Pan et al. 2014).

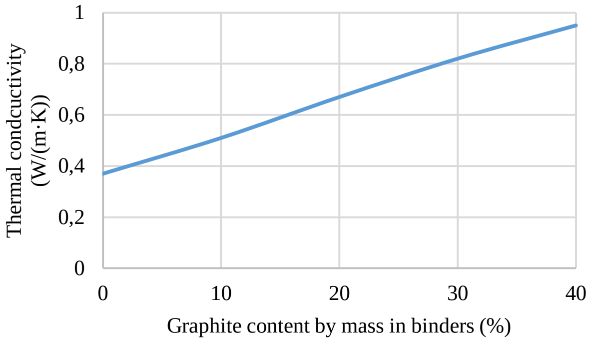

Figure 3-4. Thermal conductivity of modified binders with graphite, obtained from experimental measurments (Pan et al. 2014)

Thermal conductivity of all five different asphalt concrete types (ABT11, ABS11, AG22, ABB22 and ABS16) were numerically calculated using the modified binders with 10%, 20%, 30% and 40% graphite. The results are shown in Figure 3-5. As can be seen, the addition of 40% graphite as a filler in asphalt binder leads to a substantial thermal conductivity gains (using the numerical model). The thermal conductivity of AG22 and ABB22 increases 25% and that of ABT11, ABS11 and ABS16 increases approximately 40%, compared to the asphalt concrete without the graphite additive. ABT11, AG22 and ABB22 consist of diabase aggregates while coarse aggregates in ABS11 and ABS16 are quartzite (high thermal conductive aggregate with thermal conductivity of 5 W/(m·K)). Also, ABT11 comprises half the amount of air voids in AG22 and ABB22. This suggests that the magnitude of the effect of graphite on the thermal conductivity is significantly influenced by other parameters such as the type of aggregates and air void content. Furthermore, Figure 3-5 indicates that the thermal conductivity approximately increases direct proportional to the amount of graphite filler in the asphalt binder. The addition of 1% graphite in the binder of ABT11, AG22 and ABB22 leads to 0.01 W/(m·K) thermal conductivity gain. Also, for ABS11 and ABS16, the addition of 1% graphite in the binder of asphalt concrete leads to 0.02 W/(m·K) thermal conductivity gain.

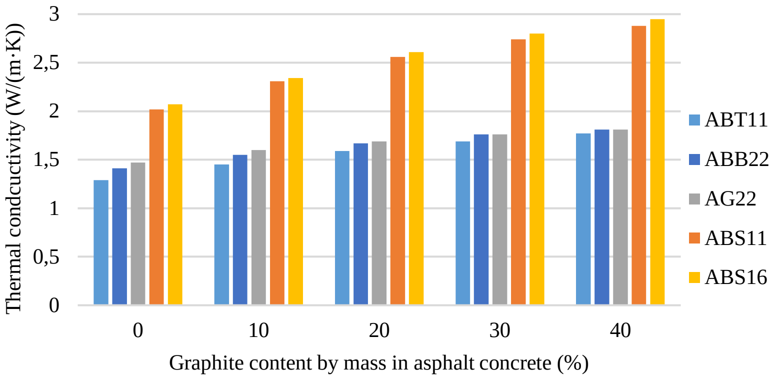

Figure 3-5. Effects of graphite on the thermal conductivity of asphalt concrete using the numerical model

4. Heat interaction between ambient and road surface

In this study, it is assumed that all snowfall is plowed away from the road surface. Hence, the supplied energy to the road surface is not used to melt snow. Also, it is assumed that the road surface should be ready (no slippery condition) for the first coming vehicle. Hence, the produced heats by vehicles such as the heats from vehicles engine and exhausted gases are not considered in the heat balances of the road surface. In addition, it is assumed that the road drainage works well enough to drain all moisture and rain from the road surface. The aim of the heating of the road surface is to mitigate the slippery condition on the road surface which occurs due to the condensation and freezing. If condensation occurs on the surface and the surface temperature is colder than freezing point (0°C), ice will be formed on the road surface.

As presented in paper I, the mass balance in this study is only based on the condensation and evaporation. Furthermore, the heat balance of the road surface consists of seven heat transfer processes namely: conductive heat from ground and pipes, q_{cond}, convective heat flow from the ambient air, q_{conv}, sensible heat from rain, q_{rain}, sensible heat from snow, q_{snow}, long-wave radiation, q_{lw}, short-wave radiation, q_{sw}, as well as latent heat of evaporation and condensation, $q_{evp/cond}$. In Figure 4-1, the heat balance of the road surface is illustrated. The heat balance of the road surface is written as:

$$q_{cond} + q_{conv} + q_{rain} + q_{snow} + q_{lw} + q_{sw} + q_{evp/con} = 0 \tag{4-1}$$

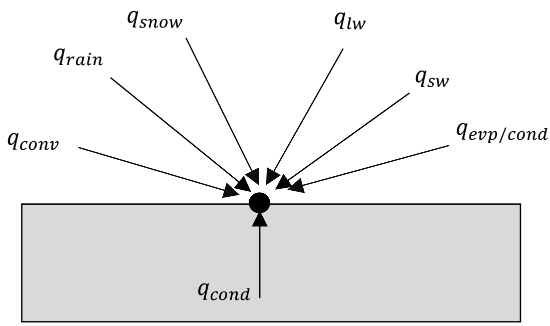

Figure 4-1. Heat balance of the road surface

It is important to note that in Figure 4-1, all of the heat fluxes directed toward the road surface, however this does not mean that they are always positive. A positive sign (+) indicates that energy is given to the surface from the ambient and a negative sign (-) indicates that energy is taken out from the surface to the ambient.

Equations related to the mass and heat balances are presented in Section 2 of paper I. Here, only the heat transfers associated with the convective heat flow between the ambient air and the road surface and long-wave radiation between the sky and the road surface are discussed in more details.

4.1.1. Convective heat flow

The convective heat flow from the ambient air to the road surface, q_{conv} (W/m^2), is calculated as (Hagentoft 2001):

$$q_{conv} = h_c.(T_{ambient} - T_{surface}) \tag{4-2}$$

where $T_{ambient}$ (K) is the ambient air temperature, $T_{surface}$ (K) is the road surface temperature and h_c (W/(m^2·K)) is the convective heat transfer coefficient. Some models used to calculate h_c are presented in Table 4-1.

In Table 4-1, v (m/s) is the wind speed, $T_{surface}$ (K) and $T_{ambient}$ (K) are the surface and the ambient air temperatures, respectively. λ_{air} (W/(m·K)) is the thermal conductivity of air, L (m) is the characteristic length of the slab in the wind direction. L considered to be 6.1 m (equal to the length of a road slab (ASHRAE 2003)), Pr is the Prandtl number for air (0.7), Re is Reynolds number based on the characteristics length (Re $= u \cdot L/\nu$), ν (m^2/s) is kinematic viscosity of air (13.2 $\cdot 10^{-6}$ m^2/s). $\rho_a c_{pa}$ (J/(m^3·K)) is the volumetric heat capacity of air (1,200 J/(m^3·K)), κ is the von Karman constant (0.4), z_0 (m) roughness length for momentum (0.01 m) and z (m) is the height above the surface.

Table 4-1. Models used to calculate the convective heat transfer coefficient

Reference	**Model**	**Eq. No.**
Hagentoft 2001	$h_c = 6 + 4 \cdot v \quad (v \le 5 \text{ m/s})$ $h_c = 7.41 \cdot v^{0.78} \quad (v > 5 \text{ m/s})$	4-3
Palyvos 2008	$h_c = 18.6 \cdot v^{0.605}$	4-4
Solaimanian, J. and Kennedy 1993; Hermansson 2004	$h_c = 698.24\left(0.00144\left(\frac{T_{surface} + T_{ambient}}{2}\right)^{0.3} \cdot v^{0.7} + 0.00097 \cdot \lvert T_{surface} - T_{ambient}\rvert^{0.3}\right)$	4-5
ASHRAE 2003	$h_c = 0.037 \cdot \left(\frac{\lambda_{air}}{L}\right) \cdot (\mathrm{Re}^{0.8} \cdot \mathrm{Pr}^{\frac{1}{3}})$	4-6
Nuijten 2016; Denby et al. 2013 (NORTRIP model)	$h_c = \frac{\rho_a c_{pa}}{r_a}$ $\frac{1}{r_a} = \frac{v_z \cdot \kappa^2}{\ln\left(\frac{z}{z_0}\right) \cdot \ln\left(\frac{10 \cdot z}{z_0}\right)}$	4-7

In paper I, Hagentoft model (Hagentoft, 2001) was used to calculated the convective heat transfer coefficient. The results showed that the difference of the annual temperature of the road surface obtained from measured data and the numerical calculation was 0.28°C with the standard deviation of 3.53°C (both measured and calculated temperature were measured at a 10 minute interval). A comparison of the different models, related to the convective heat transfer coefficient, is shown in Figure 4-2. In the calculation of the convective heat transfer coefficients, it is assumed that $T_{ambient}$ = 281.20 K and $T_{surface}$ = 283.71 K. These two values are the measured annual mean ambient air temperatures and the road surface temperature at the test site of the motorway E18 (Renman 2016). Here, it is also assumed that the wind speed varies from 0 (m/s) to 10 (m/s).

As can be seen in Figure 4-2, the different models result in different convective heat transfer coefficients. ASHRAE and Hermansson models have almost the same behavior with about 5% variations at higher wind speeds than 5 (m/s). However, at lower speeds than 5 (m/s) their values vary about 60% from each other. In NORTRIP model, the value of roughness length for momentum is very important parameter which can tremendously affect the convective heat coefficient value. In this thesis, the value of the roughness length for momentum is considered to be 0.01 m (Nuijten 2016). Having lower roughness length for momentum results in lower values for the convective heat transfer coefficient.

Generally, having higher convective heat transfer coefficient means that more heat will transfer to or from road surfaces due to the convective heat transfer. The amount of heat transfer can affect the prediction of the road surface temperature. All of the mentioned models will be examined later in Section 5.1 using a numerical model to find out their accuracy and effects on the prediction of the road surface temperature.

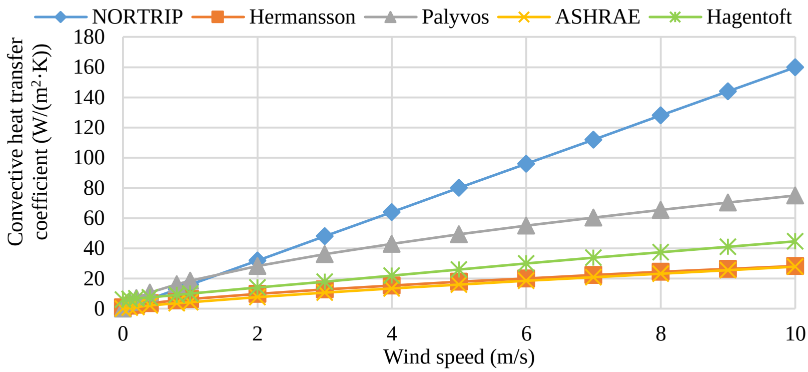

Figure 4-2. Calculating convective heat transfer coefficient at different wind speeds using five different models

Generally, the wind speed profile varies by height and will gradually reach to 0 (m/s) at the road surface due to added friction from the surface roughness. Most of the presented equations in Table 4-1 are based on experimental data. In these equations, the exact height of the wind speed measurement is not reported. The climate data, used in this study, present the wind speed at the height of 10 m (Meteotest 2010). However, the required value for the wind speed in order to calculate the convective heat transfer coefficient should be closer to the road surface. In paper I, following equation presented in (Hagentoft 2001) was used to convert the wind speed at different heights.

$$v_z = v_m \cdot k \cdot z^a \tag{4-8}$$

where v_z (m/s) is the wind speed at the height of z (m), v_m (m/s) is the wind speed at the height of 10 m and k=0.68 and a=0.17 are constant parameters for an open and flat area (Hagentoft 2001). Figure 4-3 shows the wind speed profile from 10 m height to the road surface.

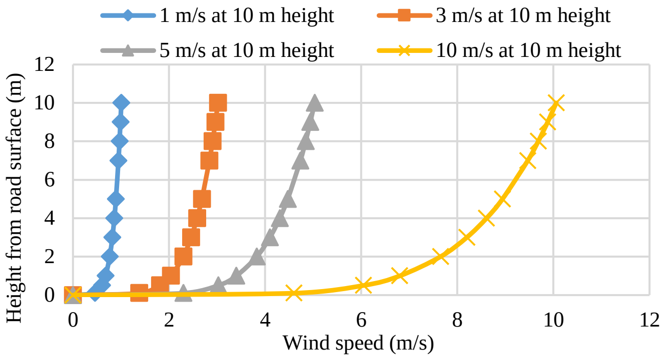

Figure 4-3. Wind speed profile at different heights above ground

4.1.2. Long-wave radiation

The long-wave radiation between the road surface and certain atmospheric constituents, q_{lw} (W/m^2), is calculated as (Theodore L. et al. 2011):

$$q_{lw} = \varepsilon \cdot \sigma \cdot (T_{sky}^4 - T_{surface}^4) \tag{4-9}$$

where ε (-) is the emissivity of the asphalt pavement surface. The values of ε ranges between 0.81 and 0.98 (Yavuzturk et al. 2005; Theodore L. et al. 2011; Dehdezi 2012; Nuijten 2016), σ ($5.67 \cdot 10^{-8}$ W/(m$^2 \cdot$ K^4)) is the Stephan-Boltzmann constant, T_{sky} (K) is the sky temperature. T_{sky} could be calculated using different models. Some of the models are presented in Table 4-2.

Table 4-2. Some models used to calculated the sky temperatures (either clear or cloudy sky)

Reference	**Model**	**Eq. No.**
Hagentoft 2001	$T_{sky} = 1.2 \cdot T_{ambient} - 14$ (clear sky) $T_{sky} = T_{ambient}$ (cloudy sky)	4-10
Hall et al. 2012	$T_{sky} = T_{ambient} \cdot \left(0.8 + \frac{T_{dew} - 273.15}{250}\right)^{0.25}$	4-11
Ramsey et al. 1999	$T_{sky} = T_{ambient} - (1.1058 \cdot 10^3 - 7.562 \cdot T_{ambient} + 1.333 \cdot 10^{-2} {T_{air}}^2 - 31.292 \cdot RH + 14.58 \cdot RH^2)$ $T_{sky} = T_{ambient}$ (cloudy sky)	4-12
Ramsey et al. 1982	$T_{sky} = 5.53 \cdot 10^{-2} \cdot (T_{ambient})^{1.5}$	4-13
Denby et al. 2013 (NORTRIP model)	$T_{sky} = T_{ambient}\left(0.23 + 0.443.\left(\frac{p}{T_{ambient}}\right)^{0.125}\right)^{0.25}$ (clear sky) $T_{sky} = 0.99 \cdot T_{ambient}$ (cloudy sky) $p = \mathrm{RH}.6.112.\exp\left(\frac{17.76.(T_{ambient} - 273.15)}{T_{ambient} - 29.65}\right)$	4-14

In Table 4-2, $T_{ambient}$ (K) is the ambient air temperature, T_{dew} (K) is the dew point temperature, RH (%) is the relative humidity and p (Pa) is the water vapor partial pressure. The abovementioned models are used to predict either the clear or fully cloudy sky temperatures. Models used to predict the partially cloudy sky temperature are not presented here due to lack of the information related to the cloud fraction in the reported data of the test site of the motorway E18 (Renman 2016).

In paper I, the sky temperature, T_{sky}, is calculated using measured incoming longwave radiation, $q_{lw-incom}$ (W/m^2). If the emissivity of the sky, ε_{sky}, is considered to be 1, then $T_{sky} = \sqrt[4]{(q_{lw-incom})/\sigma}$. The comparison of different models, related to the clear and cloudy sky temperatures, are shown in Figures 4-4 and 4-5. Figure 4-4 is related to a summer day (3rd May) and Figure 4-5 is related to a winter day (3rd January). The climate data are from the test site of the motorway E18 (Renman 2016).

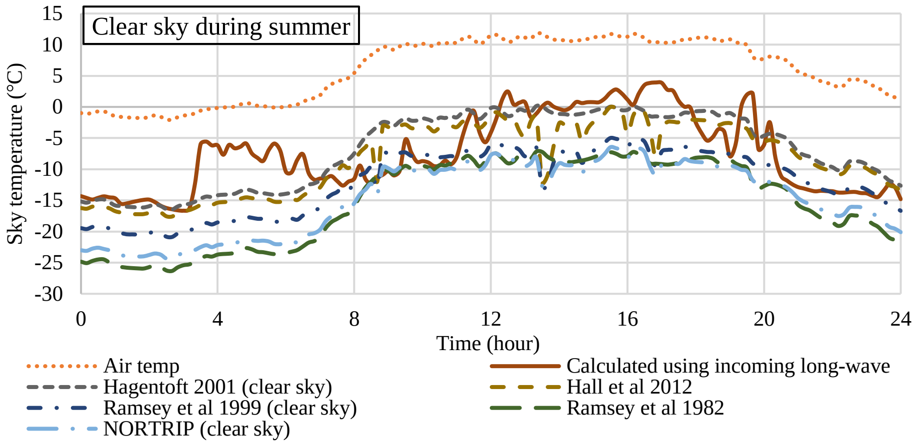

Figure 4-4. Sky temperature calculated using different models for the 3rd of May 2014 (climate data are from motorway E18 (Renman 2016))

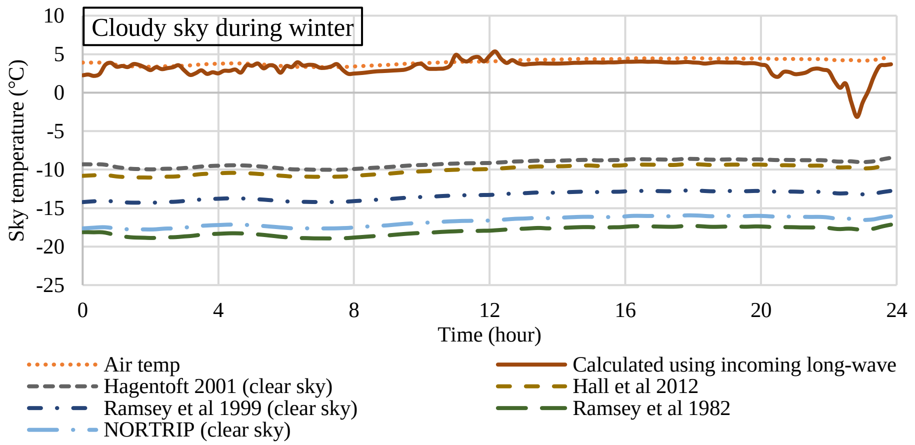

Figure 4-5. Sky temperature calculated using different models for the 3rd of January 2014 (climate data are from motorway E18 (Renman 2016))

Figure 4-4 illustrates the sky temperature during a summer day (3rd of May 2014). The calculated sky temperature is far from the ambient air temperature. Since the cloud fraction was not reported in the available data (Renman 2016), it is assumed that the sky is clear. Among all models suggested to predict the clear sky temperature in Table 4-2, Hagentoft model has the better fit with the calculated sky temperature, $\sqrt[4]{(q_{lw-incom})/\sigma}$, with the mean temperature difference of 0.46°C and the standard deviation of 4.41°C. Furthermore, as can be seen in Figure 4-5, of all models, only ambient air temperature, $T_{ambient}$, has closer fit with the calculated sky temperature. The mean difference of ambient air temperature and the calculated sky temperature for 3rd of January is 0.74°C with the standard deviation of 1.09°C. The data is related to a winter day, so it is likely that the sky is covered fully with clouds. In the models proposed by the literature (Hagentoft 2001; Ramsey et al. 1999; Denby et al. 2013), the sky temperature of the fully cloudy day is considered to be the same as the ambient air temperature.

As can be seen in both figures, the model proposed by (Ramsey et al. 1982) resulted in a cold sky temperature. The mean temperature difference between this model and the calculated sky temperature for the summer day is 7.94°C and for the winter day is 21.26°C. By comparing the different models for one day in the summer (clear sky) and one day in the winter (cloudy sky), the sky temperature obtained by Hagentoft model has a better fit with the calculated sky temperature.

5. Validation of the numerical model related to the HHP system

This section presents the validation of the numerical model associated with the HHP system. The validation are done for two cases: with and without the embedded pipes. In Section 5.1. the numerical model is validated when there is no pipe inside the road. The validation is done considering a set of measured data. In Section 5.2. the numerical model is validate when there is the embedded pipes inside the road. The validation is done considering an analytical solution. The mass and heat balances are implemented in the numerical model to predict the temperature of the road surface and the temperature at the depth of 10 cm from the surface. The numerical model is based on the FEM and made in COMSOL Multiphysics 5.2.

5.1. Validation of the numerical model using the measured temperature of a road without embedded pipes

To examine the predicted temperature of the road surface, the data of the test site of the motorway E18 (Renman 2016) was chosen because both the climate data and the measured temperature data (at different depths) were available. The climate data were: ambient air temperature (°C), dew point temperature (°C), relative humidity (%), short-wave radiation (W/m^2), incoming long-wave radiation (W/m^2) and wind speed (m/s). The precipitation data (mm/h) was not available, so the data of a nearby station from Västerås (a city close to the test-site E18) was used. In addition, the types of road layers and their thicknesses were available. However, the thermal properties of different layers and also emissivity and absorptivity of the wearing layer were not reported by (Renman 2016). In paper I, the different emissivity and absorptivity values were investigated. The results showed that $\varepsilon = 0.89$ and $\alpha = 0.78$ were suitable values for the road surface of the test site E18. The different road layers of the test site E18 and their thicknesses are shown in Figure 5-1. In Section 2.4 of this thesis, the thermal properties associated with the different asphalt concrete types were experimentally measured, see Table 2-5. The thermal properties of unbounded layers were obtained from the literatures (Eppelbaum et al. 2014; Robertson 1988; Theodore L. et al. 2011). The material properties of different road layers are listed in Table 5-1.

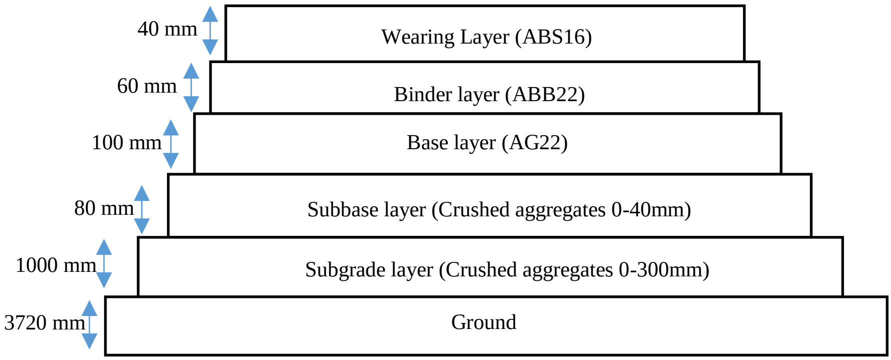

Figure 5-1. Road pavement structure of the motorway E18 (Renman 2016)

Table 5-1. Material properties associated with the different road layers of the motorway E18

References	Material	Thickness (mm)	Thermal Conductivity (W/(m·K))	Density (kg/m^3)	Specific Heat Capacity (J/(kg·K))
Experimental measurement done in this thesis (see Table 2-5)	Wearing layer (ABS16)	40	2.24	2415	848
	Binder layer (ABB22)	60	1.44	2577	822
	Base layer (AG22)	100	1.51	2582	894
Eppelbaum et al. 2014; Robertson 1988; Theodore L. Bergman et al. 2011	Subbase layer	80	0.7	1700	900
	Subgrade layer	1000	0.8	1400	900
	Ground	3720	0.6	1300	600

Long-wave and short-wave radiations, convection, evaporation, condensation and sensible rain/snow heat models were implemented to the road surface boundary. The bottom boundary at 5 m was set to be 8.05°C, equal to the annual mean temperature of the ambient air at the test site E18. The climate data were recorded at a 10 minute interval. Correspondingly, the numerical model calculated the road temperature at a 10 minute interval. The calculated sky temperature using incoming long-wave radiation, $\sqrt[4]{(q_{lw-incom})/\sigma}$, was implemented into the numerical simulation as the long-wave radiation. For convective heat transfer, the different models presented in Table 4-1 were examined to find out their effects on the predicted temperature of the road at different depths. The convective heat transfer coefficient is based on the wind speed. In the data related to the test site E18 (Renman 2016), the height of the measured wind speed was not reported. Hence, it was assumed that the wind speed was measured at the height of 10 m. The data were converted to the height of 1 m using Equation 4-8. The accumulative frequency of the wind speed at the height of 1 m associated with the test sited E18 is presented in Figure 5-2.

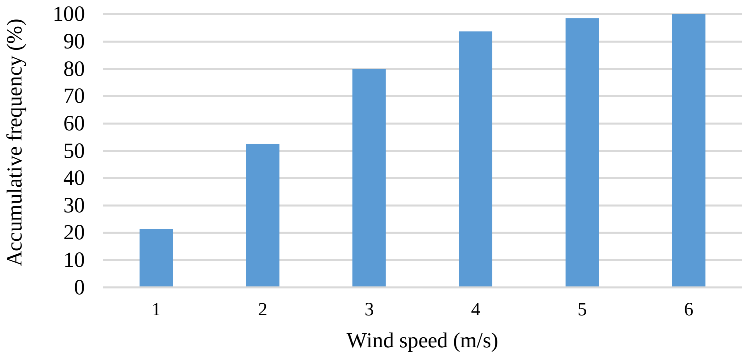

Figure 5-2. The accumulative frequency of the wind speed at the height of 1 m for the year 2014 (data are from the motorway E18 (Renman 2016))

As can be seen in Figure 5-2, for 99% of the year, the wind speed of the test site E18 at the height of 1 m is lower than 5 (m/s). One of the uncertainties in developing the numerical simulation was to select the most suitable model to calculate the convective heat transfer coefficient. The different models associate with the convective heat transfer coefficient, presented in Table 4-1, were implemented in the numerical model to predict the road temperature. The temperature was predicted on the road surface and at the depth of 10 cm from the road surface. The numerically predicted temperatures were correspondingly compared with the measured temperatures on the road surface and at the depth of 10 cm. The results of the mean temperature difference and the standard deviation between numerically predicted and measured data are presented in Tables 5-2 and 5-3.

Table 5-2. Mean difference and standard deviation of the road surface temperature (°C) between the numerical model and the measured data for the test site of the motorway E18 using different convective heat transfer models (T.Diff is $T_{numerical} - T_{measured}$ and S.D. is the standard deviation)

Time	**Hagentoft**		**Hermenson**		**NORTRIP**		**Palyvos**		**ASHRAE**	
Year/Month	**T.Diff**	**S.D.**	**T.Diff**	**S.D.**	**T.Diff**	**S.D.**	**T.Diff**	**S.D.**	**T.Diff**	**S.D.**
2014	0.28	3.53	1.16	3.81	-0.85	3.24	-0.77	3.3	1.75	4.08
January	-0.37	1.76	-0.25	1.71	-0.5	1.88	-0.5	1.86	-0.17	1.7
February	0.78	1.22	0.82	1.23	0.77	1.22	0.76	1.22	0.84	1.23
March	0.56	2.97	1.03	3.1	-0.09	2.63	0	2.75	1.31	3.17
April	0.74	4.62	2.08	4.85	-1.1	3.96	-0.91	4.14	2.96	5
May	0.37	4.54	1.96	4.76	-2.12	3.99	-1.71	4.09	2.96	4.89
Jun	0.62	4.56	2.46	4.81	-2.11	4	-1.83	4.07	3.73	4.96
July	0.96	5.38	3.16	5.57	-1.94	4.66	-1.77	4.81	4.67	5.69
August	0.29	4.25	1.89	4.42	-1.9	3.62	-1.7	3.82	3	4.49
September	0.13	3.95	1.42	4	-0.86	3.53	-1.06	3.7	2.38	4.07
October	-0.13	1.93	0.13	1.86	-0.31	1.98	-0.35	2.02	0.33	1.85
November	-0.26	1.15	-0.25	1.06	-0.13	1.36	-0.19	1.33	-0.21	1.02
December	-0.83	1.73	-1.13	1.67	-0.33	1.91	-0.41	1.87	-1.34	1.65

Table 5-3. Mean difference and standard deviation of temperature (°C) at the depth of 10 cm from the road surface between the numerical model and the measured data for the test site of the motorway E18 using different convective heat transfer models
(T.Diff is $T_{numerical} - T_{measured}$ and S.D. is the standard deviation)

Time	**Hagentoft**		**Hermenson**		**NORTRIP**		**Palyvos**		**ASHRAE**	
Year/Month	**T.Diff**	**S.D.**	**T.Diff**	**S.D.**	**T.Diff**	**S.D.**	**T.Diff**	**S.D.**	**T.Diff**	**S.D.**
2014	0.1	1.15	0.97	1.52	-1.03	1.65	1.56	1.97	1.56	1.97
January	0.2	1.5	0.32	1.53	0.06	1.49	0.06	1.48	0.41	1.57
February	0.62	0.54	0.65	0.51	0.6	0.63	0.59	0.62	0.67	0.51
March	0.28	0.76	0.72	0.82	-0.33	0.89	-0.24	0.85	0.97	0.93
April	0.34	0.96	1.64	1.21	-1.44	1.07	-1.25	0.97	2.5	1.49
May	-0.06	1.27	1.51	1.28	-2.51	1.78	-2.11	1.5	2.51	1.43
Jun	0.2	1.22	2.03	1.37	-2.53	1.48	-2.24	1.28	3.28	1.54
July	0.31	1.22	2.47	1.38	-2.54	1.53	-2.38	1.26	3.95	1.6
August	0.15	0.86	1.76	0.96	-2.05	0.95	-1.85	0.87	2.87	1.08
September	0.01	0.82	1.3	1.01	-1.02	0.87	-1.21	0.82	2.26	1.26
October	-0.22	0.65	0.07	0.6	-0.42	0.87	-0.47	0.85	0.3	0.65
November	-0.32	0.53	-0.27	0.45	-0.23	0.72	-0.29	0.7	-0.21	0.44
December	-0.84	0.98	-1.12	0.96	-0.38	1.09	-0.45	1.06	-1.31	0.97

From Table 5-2, the mean temperature difference between the numerical results and the measured data (T.Diff.) of the road surface using the Hagentoft model (for the convective heat transfer coefficient) fits better with the measured data (the annual T.Diff.= 0.28°C with S.D.=

3.53°C). It is interesting to note that the calculation of the convective heat transfer coefficient using Hagentoft model has better fit for warm days (from April to September). Among all models, Nortrip model has lower T.Diff. (on average about 0.18°C) for March, November and December.

Furthermore, as can be seen in Table 5-3, the results related to Hagentoft, Hermenson and ASHRAE models (for the convective heat transfer coefficient) show that the annual T.Diff. at the depth of 10 cm is approximately 0.2°C lower than that on the road surface, see Table 5-2. Also, the annual S.D. for all models at the depth of 10 cm is lower (on average about 1.95°C) than that on the road surface. Of all models, related to the convective heat transfer coefficients, Hagentoft model has the lowest annual T.Diff. equal to 0.1°C and S.D. equal to 1.15°C at the depth of 10 cm. Likewise to Table 5-2, Hagentoft model has better fit for warm days (from April to September). For cold days, Palyvos model results in lower T.Diff (on average about 0.8°C).

The Hagentoft model is selected to calculate the convective heat transfer coefficient. Climatic data are used for one winter week (10-17 February 2014) and one summer week (10-17 May 2014). The results are shown in Figure 5-3.

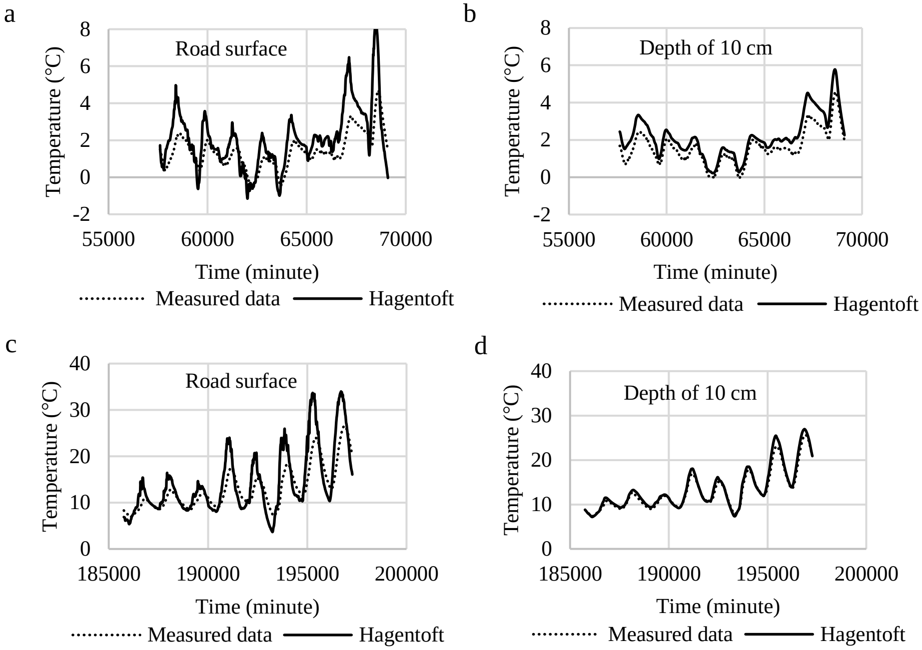

Figure 5-3. Comparison between the numerically predicted temperature and the measured data from the test site E18 (a) 10-17 February 2014 on the road surface (b) 10-17 February 2014 at the depth of 10cm for the surface (c) 10-17 May 2014 on the road surface (d) 10-17 May 2014 at 10 cm depth from the surface

As can be seen in Figure 5-3, the difference between the predicted and measured temperatures on the road surface is higher than that at the depth of 10 cm. The road surface temperature during the February period shows maximum 5°C variation between the predicted and measured data. This variation in May is about 10°C. The maximum variation of temperatures at the depth of 10 cm between the predicted and measured temperatures is about

1.5°C for both February and May periods. For all cases, the predicted temperature is higher than the measured temperatures. One reason of having warmer predicted surface could be considering a higher absorptivity value (leading to absorb more short-wave radiation on the road surface) in the numerical simulation.

The variation of the temperature on the road surface is higher than that at the depth of 10 cm. The road surface is exposed to some types of heat processes such as heats from traffic which were already neglected in this thesis. Also, the positions of sensors, installed on the road surface in order to measure the temperature of the surface, could be in question. If the sensors are exactly installed on the road surface, external loads like traffic could damage them.

5.2. Validation of the numerical model with embedded pipes using analytical solution

For the case with embedded pipes in the road, the validation was done using an analytical solution. As it is shown in Figure 5-4, a one-layer road with an embedded pipe was considered in the calculation of the thermal resistance between the pipe and road surface. The equations, associated with the analytical solution, were obtained from the literature (Hagentoft and Roots 2016) and were divided into two parts: without and with surface resistance, R_s (m^2·K/W). The equations are written as:

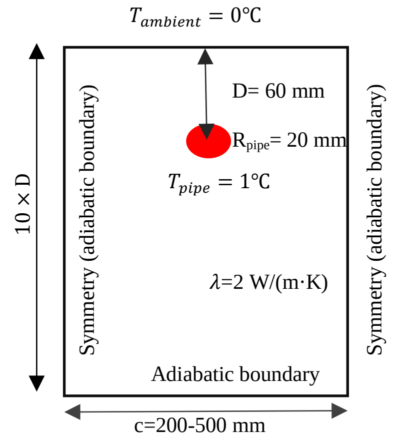

Figure 5-4. Scheme of the model used to calculate the thermal resistance between pipes and road surface

- Without surface resistance

$$R = R_0 + R_0^* \tag{5-1}$$

$$R_0 = \frac{1}{2\pi\lambda} \cdot \ln\left(\frac{2D}{R_{pipe}}\right) \tag{5-2}$$

$$R_0^* = \frac{1}{2\pi\lambda} \cdot \ln\left(\frac{c}{2\pi D} \cdot \sinh\left(\frac{2\pi D}{c}\right)\right) \tag{5-3}$$

- With surface resistance

$$R = R_0 + R_0^* + \Delta R_0 + \Delta R_0^* \tag{5-4}$$

$$\Delta R_0 = \frac{1}{\pi\lambda} \cdot e^{\frac{2D}{d}} \cdot E_1(\frac{2D}{d}) \tag{5-5}$$

$$\Delta R_0^* = \frac{2}{\pi\lambda} \cdot \sum_{n=1}^{\infty} e^{v} \cdot E_1(v) + \frac{1}{\pi\lambda} \cdot e^{\frac{2D}{d}} \cdot E_1(\frac{2D}{d}) \tag{5-6}$$

$$d = R_s \cdot \lambda \tag{5-7}$$

$$E_1(v) = \int_v^{\infty} \frac{e^{-x}}{x} dx \tag{5-8}$$

$$v = \frac{2D+i \cdot nc}{d} \tag{5-9}$$

here, R (m·K/W) is the thermal resistance between the pipe and road surface, R_0 (m·K/W) is the thermal resistance of the single pipe when the distance between the pipes is infinite and R_0^* (m·K/W) is the effects of the thermal resistance from the other pipes, ΔR_0 (m·K/W) and ΔR_0^* (m·K/W) are the effects of the surface resistance respectively for a single pipe and an array of pipes. λ (W/(m·K)) is the thermal conductivity of the road, D (m) is the embedded depth of the pipe from its center to the road surface, R_{pipe} (m) is the radius of the pipe, c (m) is the distance between the pipes and R_s (m^2·K/W) is the surface thermal resistance. For more detail about the analytical solutions and equations, the reader is referred to (Hagentoft and Roots 2016).

The numerical model has the same geometry and material properties as the analytical model, see Figure 5-4. The road consists of one layer with the thermal conductivity of 2 W/(m·K). The pipe radius was 20 mm and its temperature was set to be 1°C. The distance between the pipes varies from 200 mm to 500 mm. The analytical solution is based on a semi-infinite geometry. In the numerical simulation, the height of the model was truncated to 10 times larger than the distance between the pipes. The ambient temperature was set to be 0°C. The other boundaries were adiabatic. The thermal resistance between the pipe and road surface was obtained in two cases: without surface resistance and with surface resistance. In this thesis, four different surface resistances: 0.1 m^2·K/W, 0.2 m^2·K/W, 0.5 m^2·K/W and 1 m^2·K/W were taken into consideration. The comparison of the calculated thermal resistance between the pipe and the surface using the analytical solutions and the numerical model is shown in Figure 5-5. Figure 5-5 (a) is for the case without surface resistance and Figure 5-5 (b) is for the case with surface resistance. As can be seen, the obtained results of the thermal resistance between the pipe and the surface from the numerical simulation and analytical solution have good match with each other. For the case without surface resistance, the maximum error between the analytical and numerical results is 3.3%. For the case with the surface resistance of 1 m^2·K/W, the error is less than 1%. The error is increased when reducing the thermal resistance on the road surface and having pipes closer to each other. It is also worth noting that the analytical model is based on line sources and the error compared with real circular pipes increases when the pipes are too close to each other or too close to the ground surface.

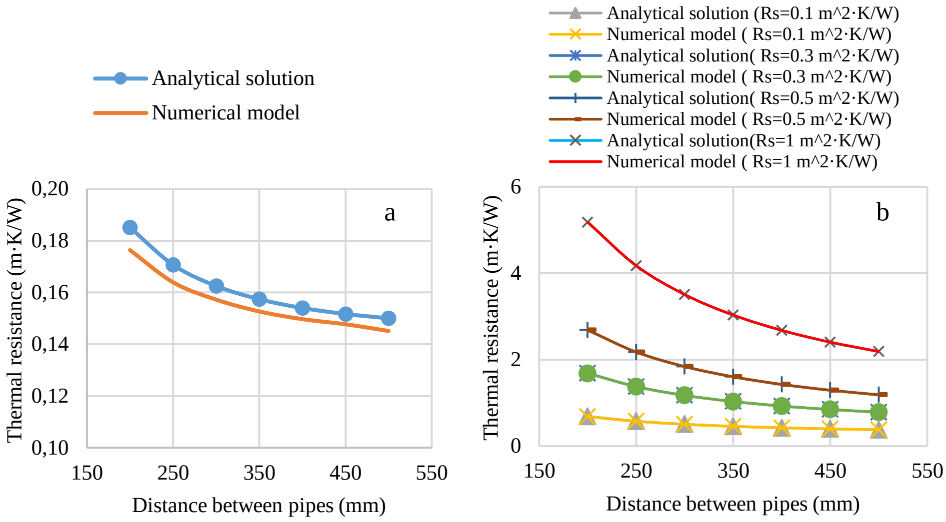

Figure 5-5. Thermal resistance between the pipe and the surface for the different pipe distances (a) without surface thermal resistance (b) with four different surface thermal resistance: 0.1 m^2·K/W, 0.2 m^2·K/W, 0.5 m^2·K/W and 1 m^2·K/W

6. Implementation of the numerical model of the HHP system using Östersund climate data

The objective of this chapter is to make a numerical model of the HHP system to investigate the anti-icing and energy harvesting processes of a road close to Östersund (63.18 N, 14.5 E). There is an ongoing project to construct a test site in 2017. The location was selected since it is an area with long and cold winters with an annual mean temperature of 2.53°C. Climate data were obtained from (Meteotest 2010). The data were recorded at a 1 hour interval and included dry-bulb/air temperature (°C), relative humidity (%), wind speed at the height of 10 m above the road surface (m/s), dew point temperature (°C), incoming long-wave radiation (W/m^2), short-wave radiation (W/m^2) and precipitation (mm/h). The numerical simulation was modeled using the implicit time-stepping method. The time-step was 1 hour in line with the climate data resolution.

The Östersund test-site is illustrated in Figure 6-1. The whole length of the test site is about 60 m and its width is about 3.5 m. The test site consists of a HHP system (Pavement 1A), coupled with Borehole Thermal Energy Storage (BTES). Also, the test site includes two electrical heating pavements (Pavement 1B and Pavement 2) and two reference pavements (Refs 1 and 2). Two different pavement types will be used in the construction of the test site. Pavement 1 and Ref 1 are a standard concrete and Pavement 2 and Ref 2 are a modified asphalt concrete, described in Chapter 3. Two reference pavements (Refs 1 and 2) are used to compare the slippery conditions and the surface temperatures in the cases with and without heating system.

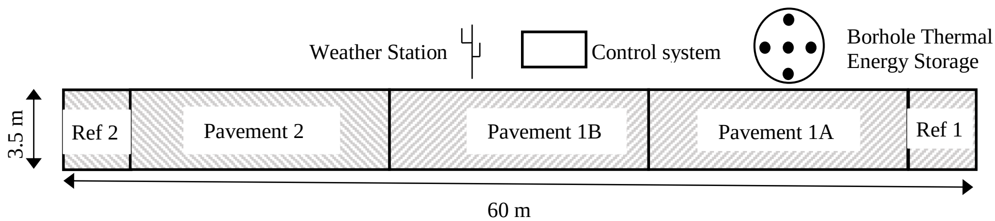

Figure 6-1. Scheme of Östersund test site with five different sections and two different pavement types. The test site includes boreholes thermal energy storages, control system and weather station (Adl-Zarrabi, et al. 2016).

6.1. HHP system for the anti-icing of the road surface

The accumulative frequency of the ambient air temperature in Östersund is shown in Figure 6-2. For about 90% of the year, the ambient air temperature varies between -12°C and 16°C. A colder road requires more amount of energy to mitigate the slippery conditions. Hence, to design the HHP system, it is of importance to have a control system to start and stop the heating of the road surface. An idea for the control system could be to stop heating the road surface for cold air temperature (for example below -12°C) and then resume the heating when the air temperature is higher than that temperature. In paper I, different air temperatures from -20°C to -8°C were examined using the numerical model. The results showed that the control strategy of stopping heating at the lower temperatures will lead to shorter slippery conditions on the road surface. However, the required energy for anti-icing the road surface will be higher. For example, considering the air temperatures of -12°C instead of -8°C to stop heating the road surface leads to 2.4 times fewer hours of the slippery conditions on the road surface, while the annual required energy for the anti-icing is about 20% higher. As can be seen in Figure 6-2, for 6% of the year, the air temperature is below -12°C. Also, in paper I (Section 5), it was concluded that for 90% of the year, the slippery condition occurs when the ambient air temperature is above -12°C. Hence, in this thesis, -12°C is considered as the lowest air temperature to stop heating the road surface.

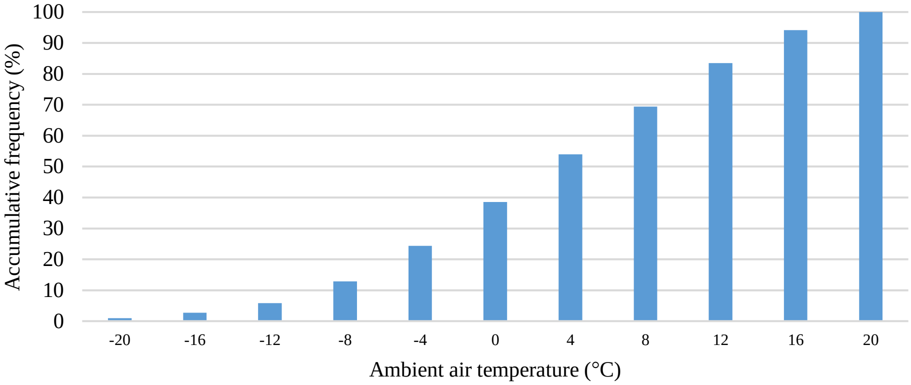

Figure 6-2. Accumulative frequency of the ambient air temperature using climate data for Östersund (Meteotest 2010).

Since the test site of Östersund has not been constructed yet, the road pavement structure is assumed to be the same as the test site of the motorway E18, see Figure 5-1. In order to simulate the HHP system, it is assumed that the embedded pipes are placed in the second (binder) layer of the road. The reason of the installing pipes in the binder layer is to reduce the risk of damage to the pipes under traffic loads. The thermal properties of the road layers are assumed to be the same as Table 5-1. In this study, the pipe types are selected as polyethylene (PEX) with the thermal conductivity of 0.4 W/(m·K), density of 925 kg/m^3 and the specific heat capacity of 2,300 J/(kg·K) (Björn 2015). The information related to the distance between pipes, the embedded depth of pipes, the outer diameter and thickness of pipes, emissivity and absorptivity of the road surface and the lowest air temperature at which the heating is stopped are presented in Table 6-1.

Table 6-1. Information associated with the studied HHP system

Parameter	**Value**	**Unit**
Thermal conductivity of pipe materials	0.4	W/(m·K)
Density of pipe materials	925	kg/m^3
Specific heat capacity of pipe materials	2300	J/(kg·K)
Outer diameter of the embedded pipes	25	mm
Pipe thickness	2.3	mm
Pipe temperature (when it is running)	6	°C
Distance between pipes	100	mm
Embedded depth (from the pipe center to the road surface)	87.5	mm
Emissivity of the asphalt layer	0.89	-
Absorptivity of the asphalt layer	0.78	-
Air temperature to stop heating	-12	°C
Thickness and properties of road materials	from Table 5-1	

Figure 6-3 illustrates a scheme of the studied HHP system. Details associated with developing the numerical model are explained in Chapters 4 and 5. The bottom boundary at the depth of 5 m is set to be 2.53°C, equal to the mean annual temperature of the ambient air.

If the surface temperature, $T_{surface}$, is lower than the dew-point temperature, T_{dew}, moisture will appear on the road surface due to the condensation. If $T_{surface}$ is lower than water freezing point, $T_{freezing}$, the moisture on the road surface will turn to ice. Therefore, the HHP system should start heating the road to keep the temperature of the road surface above the dew point temperature to prevent condensation on the road surface. In this case, even if the temperature of the road surface is lower than the freezing point, the road surface becomes ice free.

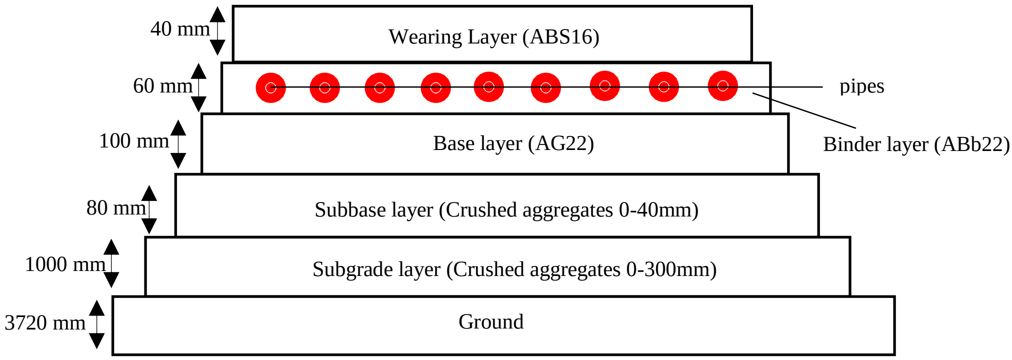

Figure 6-3. Scheme of the HHP system in a multilayer layer road

The HHP system will run when the following conditions are satisfied.

$$\begin{cases} T_{surface} < T_{dew} \\ T_{surface} < 0°\mathrm{C} \\ T_{ambient} > -12°\mathrm{C} \end{cases} \tag{6-1}$$

here, $T_{surface}$ is considered to be the temperature of the surface in the middle of the pipes. Whenever the heating is started, the temperature of the fluid, circulating through the pipes, is set to be 6°C. Furthermore, whenever the heating is stopped, the boundary condition at the inner surface of the pipe walls is set to be adiabatic. By calculating the heat flow to the surface from a single pipe, $q_{pipe-heating}$ (W/m), the annual required energy for the anti-icing of the road surface, E_r (kWh/(m·year)), is calculated as:

$$E_r = \frac{W}{c} \cdot \int_{t=0}^{1\,year} q_{pipe-heating} \cdot dt \tag{6-2}$$

where *c* (m) is the distance between the pipes and *W* (m) is the width of the road. As can be seen in Figure 6-1, *W*=3.5 m.

Furthermore, the number of hours of the slippery condition on the road surface, $t_{slippery}$ (h), is calculated when the temperature of the road surface is lower than both 0°C and dew-point temperature.

$$t_{slippery} = \int_0^{1\ year} f \cdot dt \quad \left(f = 1\ if \begin{pmatrix} T_{surface} < T_{dew} \\ T_{surface} < 0°\mathrm{C} \end{pmatrix} \text{ otherwise } f = 0\right) \qquad (6\text{-}3)$$

6.2. Effects of the different thermal properties of bounded layers on the anti-icing performance of the HHP system

In paper I, the effects of different thermal conductivity of the wearing layer on the anti-icing performance of the HHP system were investigated. The objective of this section is to investigate the effects of different thermal conductivity of all three bounded layers (wearing, binder and base layers) on the harvesting and anti-icing performances of the HHP system. Four different pavement structures with different thermal properties are taken into consideration, see Table 6-2. The thermal properties of pavement layers of Structure 1 is considered to be the same as the experimentally measured values, see Table 2-5. In Structure 2, the wearing layer is replaced with a layer with the thermal conductivity of 3 W/(m·K). This value is related to the thermal conductivity of the ABS16 sample (obtained from the numerical models) with modified binders by addition of 40% graphite, see Figure 3-5. In Structure 3, both the wearing and binder layers are replaced with the modified ABS16. In Structure 4, all of three bounded layers are replaced with the modified ABS16. The density and specific heat capacity of the modified ABS16 is considered to be 2,415 kg/m^3 and 848 J/(kg·K), respectively.

Table 6-2. Different pavement structures with different thermal properties used to investigate the effects of using high thermal conductive asphalt layers on the harvesting and anti-icing performances of the HHP system

Pavement structure	Thermal conductivity (W/(m·K))		
	Wearing layer	Binder layer	Base layer
Structure 1	2.24	1.44	1.51
Structure 2	3	1.44	1.51
Structure 3	3	3	1.51
Structure 4	3	3	3

Considering the abovementioned conditions and boundaries, the developed numerical model was run using the climate data for Östersund and the data shown in Table 6-1. Four different simulations of the HHP system were correspondingly done for each of the pavement structures in Table 6-2. The results associated with the annual required energy for the anti-icing and also total hours of the remaining slippery conditions on the road surface are shown in Figure 6-4.

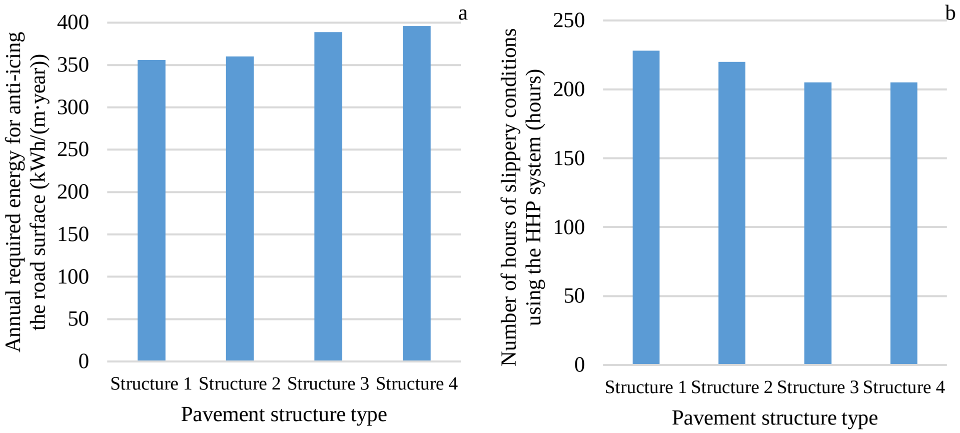

Figure 6-4. The effects of enhancing the thermal conductivity of the different layers of the road including the HHP system on (a) the annual required energy for anti-icing (b) the remaining slippery hours on the road surface (the climate data are related to Östersund)

As can be seen in Figure 6-4 (a), the annual required energy associated with Structure 2 is approximately 2% higher than that related to Structure 1. In addition, Figure 6-4 (b) shows that Structure 2 results in 8 hours fewer slippery conditions on the road surface, compared to Structure 1. Furthermore, replacing both wearing and binder layers with a layer with higher thermal conductivity (Structure 3) and also replacing all asphalt pavement layers with a layer with higher thermal conductivity (Structure 4) result in about 10% higher annual required energy for anti-icing the road surface compared to Structure 1. The number of hours of the slippery conditions associated with Structures 3 and 4 is 23 hours fewer compared to Structure 1. In this study, the embedded pipes are installed in the binder layer. In Structures 3 and 4, the thermal conductivity of the binder layer is enhanced which leads to an increase in the amount of the heat transfers from the embedded pipes to the road surface. Comparing Structure 3 and Structure 4 proves that enhancing the thermal conductivity of the third layer results in 2% more annual required energy and no significant change in the number of hours of the slippery conditions.

6.3. Asphalt solar collectors

The objective of this section is to find out the annual harvested energy and the temperature decrease of the road surface by running the HHP system in the summer. It is important to mention that based on the Östersund data, for 30% of the year, the ambient air temperature is above 8°C. Moreover, for about 70% of the warm days (from the first of May to the end of September), the air temperature is higher than 8°C. In this thesis, the air temperature of 8°C is considered as the harvesting control temperature of the HHP system. The HHP system will harvest energy when the following condition is satisfied:

$$T_{ambient} > 8°\text{C} \tag{6-4}$$

In the numerical simulation, whenever the HHP system is started to harvest energy, the temperature of the fluid, circulating through the pipes is set to be 6°C. In addition, whenever the running is stopped, the boundary conditions at the inner surface of the pipe walls is set to be adiabatic.

By calculating the heat flow, $q_{pipe-harvesting}$ (W/m), from the road surface to a single pipe during the harvesting period, the annual harvested energy, E_h (kWh/(m·year)), is calculated as:

$$E_h = \frac{W}{c} \cdot \int_{t=0}^{1\,year} q_{pipe-harvesting} \cdot dt \tag{6-5}$$

Furthermore, the calculation of the surface temperature with and without the HHP system makes it possible to detect the temperature decrease of the road surface at the summer.

Considering the air temperature above 8°C to start harvesting will lead to less harvested energy from the road surface. For example, considering the air temperature of 12°C instead of 8°C to start harvesting the energy from the road surface results in about 30% less annual harvested energy. Moreover, considering lower air temperatures to start harvesting does not prove a significant increase in the annual harvested energy. For example, considering the air temperature of 6°C instead of 8°C to start harvesting energy results in 3% higher annual harvested energy.

The four pavement structures presented in Table 6-2 are taken into consideration to find out the influence of enhancing the thermal conductivity of the road layers on the harvesting performance of the HHP system. Figure 6-5 illustrates the annual harvested energy and the mean temperature decrease of the road surface during the warm days. As can be seen, the results associated with both the annual harvested energy and the mean temperature change prove the better performance of Structures 3 and 4, compared to Structures 1 and 2. By replacing only the wearing layer with a high thermal conductive asphalt concrete (Structure 2), the annual harvested energy increases 4% and the mean surface temperature decreases 0.3°C. If the replacement is done for the both wearing and binder layers (Structure 3), the increase in the annual harvested energy will be 25% and the decrease in the mean surface temperature will be 1.5°C, compared to Structure 1. Enhancing the thermal conductivity of all asphalt pavement layers (Structure 4) compared to Structure 3, does not prove a significant change in both annual harvested energy (less than 1%) and the mean temperature decrease of the road surface.

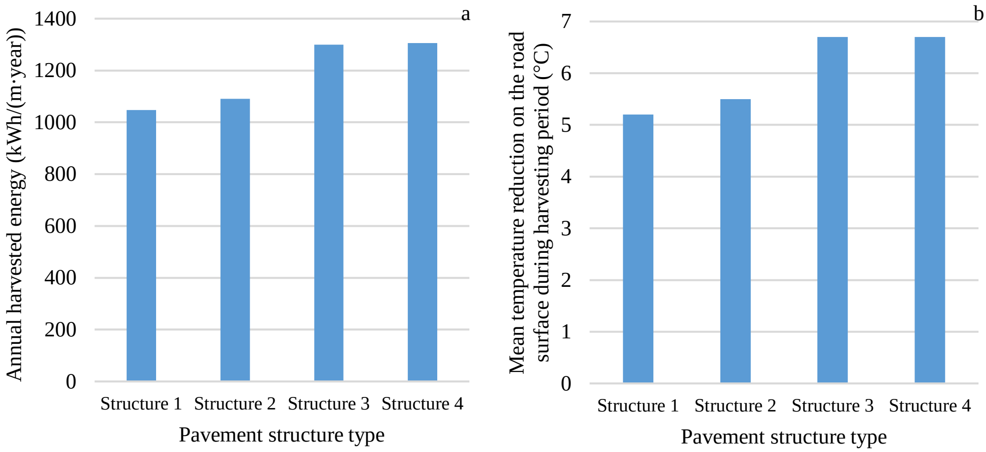

Figure 6-5. The effects of enhancing the thermal conductivity of the different layers of the road including the HHP system on (a) the annual harvested energy (b) the mean temperature reduction of the road surface (the climate data are related to Östersund)

The amount of annual harvested energy during warm days is higher than the annual required energy for anti-icing the road surface during cold days. The energy difference between harvesting and anti-icing periods for Structures 1 and 2 is approximately 700 kWh/(m·year) and for Structures 3 and 4 is approximately 900 kWh/(m·year).

.

7. Summary and conclusion

The project of "safe and ice free roads using renewable energy", investigates the possibility of utilizing harvested solar energy for deicing the road surfaces during winter to increase the road safety. A traditional method to mitigate the slippery conditions on the road surface is to spread out sand and salt. This method results in corrosion of the road infrastructures and damage to surrounding vegetation. An alternative sustainable method, for anti-icing the road surface is to use a Hydronic Heating Pavements (HHP). The HHP system consists of embedded pipes inside the road. The HHP system works based on the heat transfer between the embedded pipes and the road surface. Hence, the thermal properties of the road materials will play an important role in the efficiency of the HHP system. In this thesis and paper II, the thermal properties of the five typical asphalt concrete types, used in Sweden to construct the road, were measured using the TPS method. The measurements were done by different TPS sensor sizes. The results showed that when the ratio of the sensor size to the maximum aggregate size was higher than 2, the accuracy of thermal measurements was improved. Furthermore, in order to detect the effects of the different design parameters such as the aggregate types and air voids of asphalt concrete on the thermal properties, a 2-D numerical model of the asphalt concrete was developed. The shapes of aggregates and air voids were considered to be circular cross-section. The comparison between the obtained thermal properties from the numerical model and experimental measurements showed that the relative error between two methods was in the range of 2% to 10%. The developed numerical model was used to investigate the effects of design parameters of asphalt concrete such as air void content, modified binders with graphite, aggregate type and gradation on the thermal properties of asphalt concrete. The results revealed that considering lower air void content and dense gradation, using quartzite aggregate and the modified binder with graphite could result in 40% gain in the thermal conductivity of asphalt concrete.

Different models were introduced to calculate the convective heat transfer coefficient and the sky temperature. A numerical model of a road, the motorway E18 in Sweden (Renman 2016), was simulated to detect the most suitable models associated with the convective heat transfer coefficient and the sky temperature. The motorway E18 was selected because both the climate data and the measured temperature of the road at different depths were available. The results of the numerical model showed that, among all models of the convective heat transfer coefficient, the model proposed by Hagentoft (2001) resulted in the lowest mean annual temperature difference on the road surface, equal to 0.28°C with the standard devotion of 3.53°C between the measured data and the calculated temperatures. In addition, results related to the sky temperature showed that, among all models suggested to calculate the clear sky temperature, the model proposed by (Hagentoft 2001) fitted better with the calculated sky temperature with the mean temperature difference of 0.46°C and the standard devotion of 4.41°C.

In order to investigate the harvesting and anti-icing performances of the HHP system, the climate data was selected from Östersund in middle of Sweden, where there is an ongoing test site project to construct the HHP system in 2017. The climate data was a one-year generated data from (Meteotest 2010). In this study, the effects of enhancing the thermal conductivity of road layers on the performance of the HHP system were investigated. The results showed that replacing whole asphalt layers of the road with a high thermal conductive layer resulted in 10% decrease in the remaining hours of the slippery conditions on the road surface during the anti-icing operation of the HHP system. In addition, using the high thermal conductive asphalt concrete for all layers of the road resulted in 10% higher annual required energy for anti-icing the road surface from 356 kWh/(m·year) to 396 kWh/(m·year). Also, using the high thermal conductive asphalt concrete for all layers of the road resulted in 25% increase in the harvested energy from 1,047 kWh/(m·year) to 1,305 kWh/(m·year).

8. Future work

In this thesis, the maximum obtained thermal conductivity of asphalt concrete was 3 W/(m·K), using the numerical model of the asphalt concrete microstructure. The future study can investigate the possibility of enhancing the thermal conductivity of asphalt concrete. For example, it should be examined how using slag aggregates to fabricate asphalt concrete can influence the thermal conductivity.

Furthermore, the results of this study showed that the difference between the harvested energy from the road surface and the required energy for anti-icing the surface was about 700 kWh/(m·year). The harvested energy was higher than the required energy for anti-icing. However, in practice there are energy losses in the storage and pipes. In the future work, it should be checked whether or not the saved energy in the storage is enough to melt ice/snow on the road surface. The snow melting should be considered based on two conditions: when snow is plowed away and only slush remains on the road surface and when there is no plowing system; i.e. snow remains on the road surface.

The control system of the HHP system is an important parameter which can affect the efficiency of the HHP system. The future study should investigate a more effective control system; e.g. fluids with different temperatures should pump through the pipes when the ambient conditions varies. In this study, the effects of different parameters related to the HHP system were examined on the anti-icing performance of the HHP system. However, the investigation was done individually for each parameter. In future work, it is necessary to find out the combined effect of the parameters on the efficiency of the HHP system, e.g. the influence of enhancing the thermal conductivity of road layers and reducing the fluid temperature on the efficiency of the HHP system. In addition, in order to minimize the required energy and running time of the HHP system for anti-icing the road surface, optimized steering of the HHP using weather prognoses is an interesting research area. It is needed to investigate the influence of the selected time-stepping for the implicit method, in the numerical simulation, on the annual required energy for anti-icing. Preliminary investigation showed an influence when changing the time-stepping. e.g. smaller time-step than 1 hour resulted in lower annual required energy and larger time-step than 1 hour resulted in higher annual required energy. It is also needed to examine the numerical simulation using both implicit and explicit methods to find out their effects on the results.

Finally, the obtained data from the test site of Östersund will be of interest to validate the numerical model and also to develop the HHP system performance under real conditions.

References

Adl-Zarrabi, B., Johnsson, J. & Mirzanamadi, R., 2016. Hydronic Pavement Using Low Temperature Borehole Thermal Energy Storage. In *The 2016 Word Congress on Advances in Civil, Environmental and materials research (ACEM16)*. Jeju Island, Korea.

Adl-Zarrabi, B., Mirzanamadi, R. & Johnsson, J., 2016. Hydronic Pavement Heating for Sustainable Ice-free Roads. *Transportation Research Procedia*, 14, pp.704–713. Available at: http://linkinghub.elsevier.com/retrieve/pii/S2352146516303428.

Andersland, O.B., Ladanyi, B. & ASCE, 2003. *Frozen Ground Engineering, 2nd Edition*, USA: John Wiley & Sons.

Andolfsson, T., 2013. *Analyses of Thermal Conductivity from Mineral Composition and Analyses by Use of Thermal Conductivity Scanner A Study of Thermal Properties in Scanian Rock Types*. Geology department at Lund University, Master's thesis.

Apeagyei, A.K., Grenfell, J.R.A. & Airey, G.D., 2014. Evaluation of Moisture Sorption and Diffusion Characteristics of Asphalt Mastics Using Manual and Automated Gravimetric Sorption Techniques. *Journal of Material in Civil Engineering*, 26(8), pp.1–12.

ASHRAE, 2003. *ASHRAE Handbook—HVAC Applications, American Society of Heating, Refrigerating and Air Conditioning Engineers - 2003 - Chapter 50 - Snow Melting and Freeze Protection*, Atlanta, USA.

ASTM standard, 2010. ASTM D 5229– 92 – Standard Test Method for Moisture Absorption Properties and Equilibrium Conditioning of Polymer Matrix Composite Materials. *Annual Book of ASTM Standards*, 92(Reapproved), pp.1–13.

Björn, M.O., 2015. *Sammanställning av Egenskaper för Olika Rörtyper (in Swedish)*, Östersund, Sweden.

Bobes-Jesus, V. et al., 2013. Asphalt Solar Collectors: A Literature Review. *Applied Energy*, 102, pp.962–970.

Chen, J. et al., 2013. Determination of Effective Thermal Conductivity of Asphalt Concrete with Random Aggregate Microstructure. *Journal of Materials in Civil Engineering*, 27(12), pp.1–9.

Chen, J. et al., 2015. Evaluation of Thermal Conductivity of Asphalt Concrete with Heterogeneous Microstructure. *Applied Thermal Engineering*, 84, pp.368–374. Available at: http://dx.doi.org/10.1016/j.applthermaleng.2015.03.070.

Chen, M., Wan, L. & Lin, J., 2012. Effect of Phase-Change Materials on Thermal and Mechanical Properties of Asphalt Mixtures. *Journal of Testing and Evaluation*, 40(5), p.20120091.

Côté, J., Grosjean, V. & Konrad, J.-M., 2013. Thermal Conductivity of Bitumen Concrete. *Canadian Journal of Civil Engineering*, 40(2), pp.172–180.

Dehdezi, P.K., 2012. *Enhancing Pavements for Thermal Applications*. PhD Thesis, The University of Nottingham, Transportation Engineering Centre.

Denby, B.R. et al., 2013. A Coupled Road Dust and Surface Moisture Model to Predict Non-Exhaust Road Traffic Induced Particle Emissions (NORTRIP). Part 2: Surface Moisture and Salt Impact Modelling. *Atmospheric Environment*, 81, pp.485–503.

EGEC– European Geothermal Energy Council, 2007. *Geothermal Heating and Cooling Action Plan for Europe (K4RES-H)*, Brussels, Belgium. Available at: https://ec.europa.eu/energy/intelligent/projects/sites/iee-projects/files/projects/documents/k4res-h_geothermal_heating_and_cooling_action_plan.pdf.

Ellevset, O., 2014. Norwegian Coastal Highway Route E39- Status Overview. In *Bridges Annual Conference*. Oslo, Norway: Springer.

Eppelbaum, L., Kutasov, I. & Pilchin, A., 2014. Applied Geothermics. In *Applied Geothermics*. Springer. Available at: http://link.springer.com/10.1007/978-3-642-34023-9.

Eugster, W.J., 2007. Road and Bridge Heating Using Geothermal Energy. Overview and Examples. In *Proceedings European Geothermal Congress*. Unterhaching, Germany 30 May-1 June 2007.

Gao, Q. et al., 2010. Experimental Study of Slab Solar Collection on The Hydronic System of Road. *Solar Energy*, 84(12), pp.2096–2102.

Gustafsson, M., 2013. *Instruction Manual of Hot Disk Thermal Constants Analyser Software version 5.9*, Götenburg, Sweden.

Gustafsson, S.E., 1991. Transient Plane Source Techniques for Thermal Conductivity and Thermal Diffusivity Measurements of Solid Materials. *Review of Scientific Instruments*, 62(3), p.797.

Hagentoft, C.-E., 2001. *Introduction to Building Physics* 1:7., Lund, Sweden: Studentlitteratur.

Hagentoft, C.-E. & Roots, P., 2016. Design Rules for Floor Heating System Using New Analytical Formulas. In *CESBP Central European Symposium on Building Physics and BauSIM 2016*. Dresden, pp. 23–28.

Hall, M.R. et al., 2012. Influence of the Thermophysical Properties of Pavement Materials on the Evolution of Temperature Depth Profiles in Different Climatic Regions. *Journal of Materials in Civil Engineering*, 24(1), pp.32–47.

Hermansson, Å., 2004. Mathematical Model for Paved Surface Summer and Winter Temperature: Comparison of Calculated and Measured Temperatures. *Cold Regions Science and Technology*, 40(1–2), pp.1–17.

Huang Yang, 2008. *Pavement Analysis and Design*, USA: Pearson Education.

Karim, M.R. & Krabbenhoft, K., 2010. New Renormalization Schemes for Conductivity Upscaling in Heterogeneous Media. *Transport in Porous Media*, 85(3), pp.677–690.

Knudsen, F. et al., 2014. *Vintertjeneste i de Nordiske land. Statusrapport 2014 (in Norwegian)* NVF-Rapporter, ed., Norge.

Liu, X., Rees, S.J. & Spitler, J.D., 2007. Modeling Snow Melting on Heated Pavement Surfaces. Part I: Model Development. *Applied Thermal Engineering*, 27(5–6), pp.1115–1124.

Loomans, M. et al., 2003. Design Tool for the Thermal Energy Potential of Asphalt Pavements. In *Eighth International IBPSA Conference*. Eindhoven, Netherlands: Building Simulation 2003, pp. 745–752.

Luca, J. & Mravira, D.M., 2005. New Measurement of Thermal Properties of Superpave Asphalt Concrete. *Journal of Material in Civil Engineering*, 17(1), pp.72–79.

Meteotest, 2010. *Meteonorm: Meteonorm, Global Meteorological Database. Handbook part II: Theory, version 6.1*, Bern, Switzerland.

Michael S. Mamlouk et al., 2005. Determination of Thermal Properties of Asphalt Mixtures. *Journal of Testing and Evaluation*, 33(2).

Nuijten, A.D.W., 2016. Runway Temperature Prediction, A Case Study for Oslo Airport, Norway. *Cold Regions Science and Technology*, 125, pp.72–84.

Pahud, D., 2008. *Simulation Tool for the System Design of Bridge Heatig for Ice Prevention with Solar Heat Stored in a Seasonal Ground Duct Store, User Manual*, Lugano, Switzerland.

Palyvos, J.A., 2008. A Survey of Wind Convection Coefficient Correlations for Building Envelope Energy Systems' Modeling. *Applied Thermal Engineering*, 28(8–9), pp.801–808.

Pan, P. et al., 2015. A Review on Hydronic Asphalt Pavement for Energy Harvesting and Snow Melting. *Renewable & Sustainable Energy Reviews*, 48, pp.624–634.

Pan, P. et al., 2014. Influence of Graphite on the Thermal Characteristics and Anti-Ageing Properties of Asphalt Binder. *Construction and Building Materials*, 68, pp.220–226.

Ramsey, J.W. et al., 1999. *Updated Design Guidelines for Snow Melting Systems*, ASHRAE Transactions Symposia, USA.

Ramsey, J.W., Chiang, H.D. & Goldstein, R.J., 1982. A Study of the Incoming Longwave Atmospheric Radiation from A Clear Sky. *Journal of Applied Meteorology*, 21(4), pp.566–578.

Renman, G., 2016. E18 Test-Site, Perfect Choice for Unique Road Research Station. Available at: http://testsitee18.se/Default.aspx.

Robertson, E.C., 1988. *Report of Thermal Properties of Rocks*, Unite state Department of the Interior Geological

Survey, Virginia, USA.

Santamouris, M., 2013. Using Cool Pavements as A Mitigation Strategy to Fight Urban Heat Island-A Review of the Actual Developments. *Renewable & Sustainable Energy Reviews*, 26, pp.224–240.

Solaimanian, J., Kennedy, T.W., 1993. Predicting Maximum Pavement Surface Temperature Using Maximum Air Temperature and Hourly Solar Radiation. *Transportation Research Record: Journal of the Transportation Research Board*, 1417, p.11.

StatensVegvesen, 2016. The E39 Coastal Highway Route. Available at: http://www.vegvesen.no/vegprosjekter/ferjefriE39/English.

Theodore L. Bergman et al., 2011. *Introduction to Heat Transfer* Sixth Edition., New York: Wiley and Sons.

Van Vliet, M.R.A. et al., 2005. Structural Viability of Shallow Depth Hollow Systems in Airfield Pavements. In *1st European Airport Pavement Workshop*. Amsterdam, Netherlands.

Xu, H. & Tan, Y., 2015. Modeling and Operation Strategy of Pavement Snow Melting Systems Utilizing Low-Temperature Heating Fluids. *Energy*, 80, pp.666–676.

Xu, Q.W. & Solaimanian, M., 2010. Modeling Temperature Distribution and Thermal Property of Asphalt Concrete for Laboratory Testing Applications. *Construction and Building Materials*, 24(4), pp.487–497.

Yavuzturk, C., Ksaibati, K. & Chiasson, A.D., 2005. Assessment of Temperature Fluctuations in Asphalt Pavements due to Thermal Environmental Conditions using a Two-Dimensional, Transient Finite-Difference Approach. *Journal of Materials in Civil Engineering*, 17(4), pp.465–475.